AD_____

AWARD NUMBER: W81XWH-09-1-0066

TITLE: In-vivo Diagnosis of Breast Cancer using Gamma Stimulated Emission Computed Tomography

PRINCIPAL INVESTIGATOR: Anuj J. Kapadia

CONTRACTING ORGANIZATION: Duke University
Durham, NC 27780

REPORT DATE: April 2011

TYPE OF REPORT: Annual

PREPARED FOR: U.S. Army Medical Research and Materiel Command
Fort Detrick, Maryland 21702-5012

# REPORT DOCUMENTATION PAGE

*Form Approved*
*OMB No. 0704-0188*



| **1. REPORT DATE** | **2. REPORT TYPE** | **3. DATES COVERED** |
|---|---|---|
| 1 April 2011 | Annual | 1 Apr 2010 – 31 Mar 2011 |

**4. TITLE AND SUBTITLE**

In-vivo Diagnosis of Breast Cancer using Gamma Stimulated Emission Computed Tomography

**5a. CONTRACT NUMBER**

**5b. GRANT NUMBER**
W81XWH-09-1-0066

**5c. PROGRAM ELEMENT NUMBER**

**6. AUTHOR(S)**

Anuj J. Kapadia

E-Mail: anuj.kapadia@duke.edu

**5d. PROJECT NUMBER**

**5e. TASK NUMBER**

**5f. WORK UNIT NUMBER**

**7. PERFORMING ORGANIZATION NAME(S) AND ADDRESS(ES)**
Duke University
Durham, NC 27708

**8. PERFORMING ORGANIZATION REPORT NUMBER**

**9. SPONSORING / MONITORING AGENCY NAME(S) AND ADDRESS(ES)**
U.S. Army Medical Research and Materiel Command
Fort Detrick, Maryland 21702-5012

**10. SPONSOR/MONITOR'S ACRONYM(S)**

**11. SPONSOR/MONITOR'S REPORT NUMBER(S)**

**12. DISTRIBUTION / AVAILABILITY STATEMENT**
Approved for Public Release; Distribution Unlimited

**13. SUPPLEMENTARY NOTES**

**14. ABSTRACT**
This project focuses on the development of a novel method of breast cancer detection called Gamma Stimulated Spectroscopy (GSS). This technique is highly sensitive to early stage metabolic changes in tumors and has the ability to quantify specific malignancy-related elements in a tumor through a quick and low dose scan. In this project, we aim to design, implement and optimize a prototype of the GSS imaging system and determine its accuracy and efficacy in breast cancer detection. In the first year of the project, we designed and assembled a preliminary prototype of the GSS system using the free-electron laser at Duke University and acquired experimental spectra from calibration phantoms of elements associated with breast cancer. In addition, we initiated the development of a Monte-Carlo simulation model of the GSS imaging system including the gamma source and detectors. In the second year of the project, we continued the development of the GEANT4 simulation to model and refine the physics interactions governing GSS and investigated advanced detector systems to improve system sensitivity. In addition, we investigated the GSS radiation dose using whole body and breast dosimetry models irradiated with gamma beams. Simulated populations of breast tumor patients were scanned virtually to generate images of six individual malignancy-related trace elements per phantom. The images showed excellent correlation between the location of the tumor and the concentration of the cancer-marking element in the breast. This data will now be used to identify the best candidate elements for cancer detection. In addition, we also initiated the development of a classifier algorithm to identify an optimal signature of cancer based on a combination of elements. We will now begin to optimize the GSS acquisition system for cancer detection through a targeted element search using the computer classifier algorithm.

**15. SUBJECT TERMS**
Gamma, spectroscopy, GSS, breast, tomography, imaging, MLEM, Monte Carlo simulation, Geant4

| **16. SECURITY CLASSIFICATION OF:** | | | **17. LIMITATION OF ABSTRACT** | **18. NUMBER OF PAGES** | **19a. NAME OF RESPONSIBLE PERSON** |
|---|---|---|---|---|---|
| | | | | | USAMRMC |
| **a. REPORT** | **b. ABSTRACT** | **c. THIS PAGE** | | | **19b. TELEPHONE NUMBER** *(include area code)* |
| U | U | U | UU | | |

## Table of Contents

## INTRODUCTION

Breast cancer is the leading type of cancer to affect women all over the world [1]. Early detection has proved to be highly beneficial in increasing survival rates for patients suffering from the disease. X-ray mammography, the only FDA approved screening tool for early detection, has demonstrated considerable success in the early identification of breast cancer. However, despite its considerable success, it suffers from several critical limitations due to its anatomic approach. First, it requires excellent contrast in the mammograms, which is often difficult to achieve in women with dense breasts. Second, it requires the abnormality to have developed to a stage where it is clearly visible; development that is usually observed in advanced stages of cancer. Finally, the technique has limitations in classifying a detected abnormality as benign or malignant.

We propose to overcome these limitations by developing a new and innovative imaging technique that is sensitive to a very early molecular signature of breast cancer – the difference in trace element concentration between benign and malignant tissue. Several experiments have demonstrated differences in element concentrations between benign and malignant tissue [2-12]. When illuminated with suitable radiation, most of these elements emit characteristic gamma photons that can be measured with a gamma spectrometer and can be used to diagnose malignancy. In this project, we will investigate the feasibility of detecting each of these elements in breast tissue through a new imaging method called gamma-stimulated spectroscopy and to identify the optimal set of biomarker elements that will enable accurate cancer diagnosis with minimum patient dose.

**Principle:** Gamma Stimulated Spectroscopy (GSS) uses the principle of nuclear resonance scattering (NRS) to image element concentrations in the breast. NRS [15] is a process of resonant excitation of nuclear states by absorption of electromagnetic radiation and subsequent decay of these levels by re-emission of the equivalent radiation. A gamma photon with suitable energy will excite a target atomic nucleus to a higher energy state that is often short-lived. The excited nucleus will then rapidly de-excite to a lower state with the emission of characteristic gamma radiation. The energy of the emitted gamma radiation is a unique characteristic of the element and can be used to quantitatively identify the element. The advantage of the NRS technique is that the excitation and de-excitation processes occur via the electromagnetic interaction, which is the best-understood interaction in physics. The energy of the incident gamma photon must be equal to the energy of the nuclear state to be excited plus restore losses from recoils in the nucleus [15]. The loss from nuclear recoil can be restored through Doppler effects by increasing the relative velocity of the source particle with respect to the scatterer. However, as the tolerance in the allowable spread of incident energy is small (~1ev), the number of elements that have been imaged through NRS has been limited by the availability of gamma emitters with suitable energy.

This IDEA project proposes to develop an NRS-based technique with a tunable collimated gamma source to tomographically quantify element concentrations within breast tissue. The tunable collimated gamma source available for this project can achieve very precise energy tuning over a wide range of energies, making it ideal for NRS interrogation of a large number of elements through tomographic imaging methods.

GSS presents several advantages over conventional imaging techniques. Due to its sensitivity to a very early molecular signature of breast cancer it has the potential to detect cancer at a very early stage and make a diagnosis before the development of anatomical changes that are required for diagnosis through mammography, ultrasound and MRI. It has the potential to improve the sensitivity and specificity of breast cancer detection over other non-invasive in-vivo imaging methods. It eliminates the need for breast compression, tissue excision or patient disrobing. Further, it has the ability to distinguish benign and malignant tumors without excision of tissue, which has the potential to lead to a significant reduction in the number of biopsies.

Gamma-stimulated spectroscopy (GSS) has the ability to differentiate between benign and malignant tissue through a non-invasive in-vivo scan of the breast. In our envisioned clinical implementation, an uncompressed breast will be illuminated using a collimated gamma-ray beam with energy precisely tuned to stimulate an energy state in a target nucleus. The gamma rays interacting with the target nucleus will

stimulate characteristic gamma emission through resonant behavior. The emitted gamma rays will be acquired with an energy-sensitive gamma-ray detector through tomographic acquisition and reconstructed and analyzed to quantitatively identify the location and concentration of the emitting element. Energy spectra from different projections will be evaluated using a computerized decision-making algorithm to identify volume regions containing combinations of elements associated with breast cancer. Thus, with a simple non-invasive beam scan, the GSS technique will be able to generate a tomographic image containing a three-dimensional map of volume regions in the breast with locations and characteristic of tumors identified.

## BODY

**Task 1: Acquire gamma spectra from breast tissue specimens and phantoms illuminated by a high-intensity tuned gamma beam with tomographic acquisition geometry**
(Months 1-33)

**Status:** This task has been initiated as proposed and completed in majority.

A prototype of the GSS acquisition system has been assembled on the High-Intensity Gamma Source (HIGS) facility at the Duke Free-Electron Laser Laboratory (DFELL), which is an ideal environment for initial development of the device. The acquisition system consists of a tunable gamma source, sample holder, gamma detectors, and computers for acquisition and analysis. Figures 1 and 2 show photographs of the GSS prototype system.

The system has been used to acquire data from phantoms containing breast cancer marker elements. Each of the phantoms was created approximately equal in volume to an adult the human breast. Distilled water was used in the phantom to simulate the scattering properties of tissue. The element of interest (i.e., a breast cancer marker) was added to the phantom in varying quantities. Samples of iron, copper and water were scanned with the device to provide validation data for simulation development. The energy of the incident gamma beam was selected based on the following experimental model.

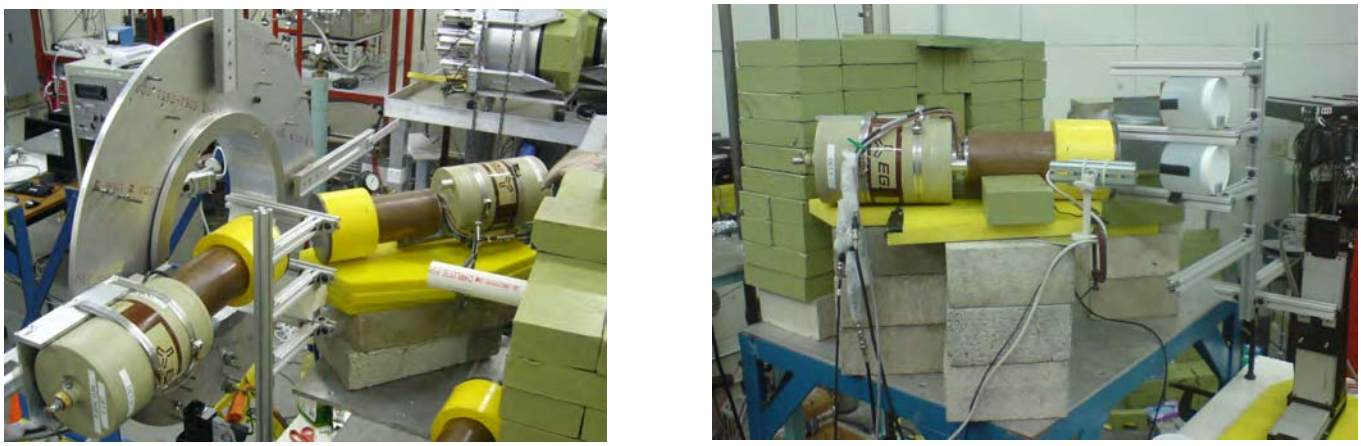

(a) (b)

**Figure 1. (a)** Photograph of the GSS prototype system developed at Duke University. The beam enters through the white plastic pipe on the right side of the image and moves towards the left. Two HPGe gamma-ray detectors (cylinders with yellow shields around them) are mounted at different angles around the sample. Each detector contains a dewar to house liquid-nitrogen ($LN_2$) required for cooling the crystal. The sample (not present in this image) is mounted on the sample-actuator that can be controlled remotely. An internet-ready camera is used to monitor the position of the sample in real-time. **(b)** A side-view of the gamma-ray detector and target samples. The samples in this image are cylindrical plastic jars containing a mixture of water and the element of interest. Several samples are attached to a mount that is controlled remotely using a sample-actuator (visible at the bottom right corner of the image). The actuator facilitates precise positioning of different samples in the beam in real-time without the need to stop/start the gamma source (which is a somewhat lengthy and time-consuming process). Also visible in this image is the camera used to monitor sample- position.

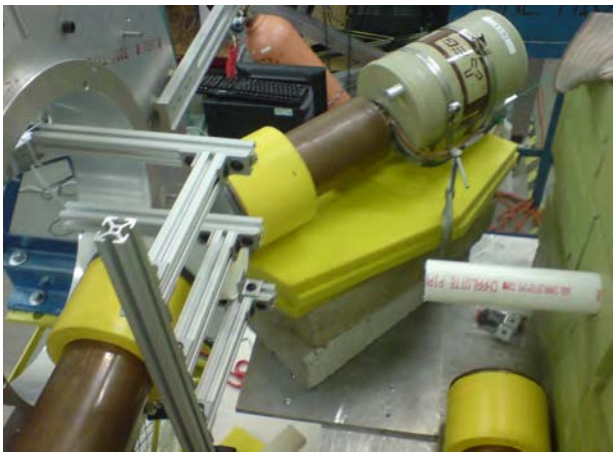

**Figure 2. (a)** Close-up of the beam entry onto the sample. The beam enters through the plastic pipe surrounded by lead shield blocks (green), which shield the sample and detectors from scattered radiation originating from the gamma-source. **(b)** Close-up of the sample-mount with three samples attached simultaneously. The sample-actuator (not visible here) is capable of moving the mount along the horizontal and vertical axes, which enables precise positioning of the gamma beam on each phantom separately. Also visible in this image is the camera used to monitor the sample-position in real-time.

**The GSS experimental model:** A gamma photon, incident on a body, travels freely along its projected path until it interacts with an atomic nucleus. If the energy of the photon is within the resonance energy window for a state in the atomic nucleus, the nucleus gets excited to that particular higher-energy state. This excited nucleus then rapidly decays to a lower state, emitting a gamma ray photon with energy equal to the difference between the two states. Detection and analysis of the emitted gamma ray spectrum enables identification and quantification of the target atom. An energy-sensitive gamma detector is used to capture the emitted gamma photons. The resonance energy window of most energy levels in a nucleus is extremely small (typically less than a few eV). Therefore, through precise tuning of the gamma beam energy, it is possible to selectively excite a single energy level in a specific element of interest in the body. Three energy states in two different elements were targeted: **3.448 MeV** in $^{56}$Fe; **6.927 MeV** in $^{56}$Fe; and **6.927 MeV in $^{16}$O**. For each of these states, the beam energy was tuned to closely match the energy of the particular state to be excited. Data were obtained from each of these samples and are shown in Figures 3 and 4.

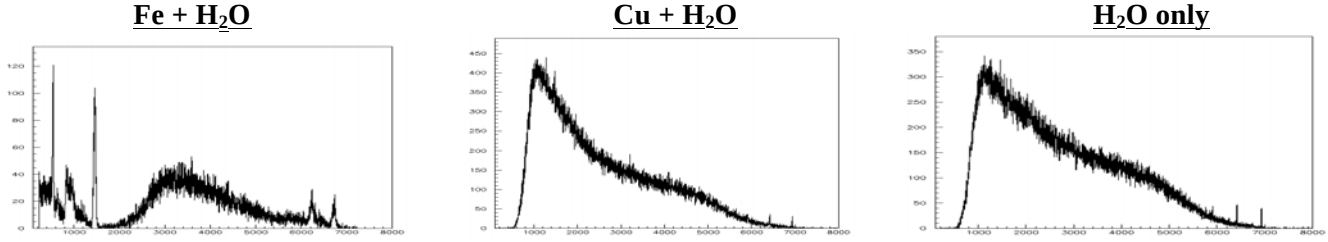


**Figure 3. (a)** GSS spectrum from a sample of iron and water obtained using a 6.9 MeV gamma beam. A prominent gamma line is visible at 6.9 MeV (primary peak) and at 6.4 MeV (first escape). These lines are due to interactions with energy states in both iron and oxygen in the sample. **(b)** GSS spectrum from a sample of copper and water obtained using a 6.9 MeV gamma beam. Gamma lines are visible at 6.9 MeV (primary peak) and at 6.4 MeV (first escape). These lines are due to interactions with energy states in oxygen in the sample. The gamma line at 6.9 MeV is visibly narrower than in the case of the sample with iron. **(c)** GSS spectrum from a sample of pure distilled water obtained using a 6.9 MeV gamma beam. Gamma lines are visible at 6.9 MeV (primary peak) and at 6.4 MeV (first escape). These lines are due to interactions with energy states in oxygen in water. The gamma line at 6.9 MeV is visibly narrower than in the case of the sample with iron.

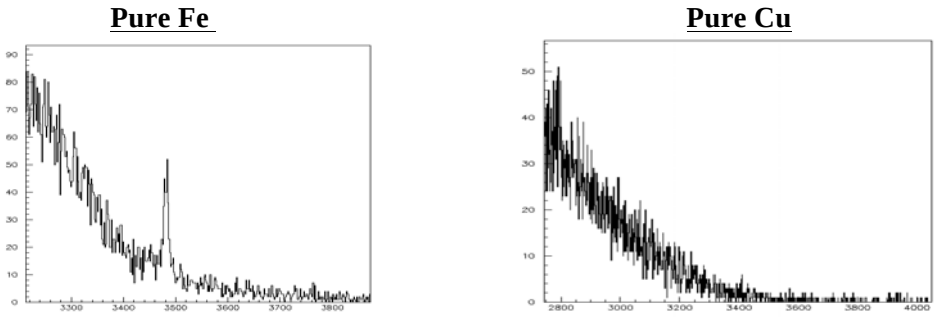


**Figure 4. (a)** GSS spectrum from a sample of pure natural iron obtained using a 3.5 MeV gamma beam. A prominent gamma line is visible at 3.48 MeV, which is due to interactions with the 3.448 energy state in iron. **(b)** GSS spectrum from a sample of pure natural copper obtained using a 3.5 MeV gamma beam. Copper does not contain any energy levels that are close to 3.5 MeV, and therefore, no nuclear resonance is created in this sample. The spectrum from this sample further demonstrates the validity of the technique for quantification of a single element (i.e., the gamma line is present in Fig 4a and absent in Fig 4b).

**Task 2: Design computerized classifier model for detection and diagnosis of breast cancer.** (Months 13-33)

**Status:** This task has been initiated and is currently under way.

Breast cancer has been associated with a variety of elements that differ between benign, malignant and normal tissue. These elements include Al, Br, Ca, Cl, Co, Cs, Cu, Fe, K, Mn, Na, Rb, and Zn. Given the large number of elements that can be targeted, identifying an appropriate combination of elements to detect cancer effectively and accurately is an important task. GSS is a targeted stimulation technique; i.e., the gamma energy can be precisely controlled to stimulate a specific element within the body. Further, each element exhibits a different nuclear resonance cross-section and emits gamma photons of a different energy, both of which result in a different overall detection efficiency for the element. Therefore, in this task, we aim to determine the best element or set of elements that can be stimulated, detected and quantified most effectively and accurately. The implementation of the algorithms is a relatively simple task. The accuracy of the results depends on the strength of the database, which is currently being generated.

**Task 3: Optimize acquisition strategy using a Monte Carlo model of the acquisition system.** (Months 15-30)

**Status:** This task has been initiated and is currently under way.

A simulation of the NRF process does not currently exist in GEANT4. In year 1 of the project, we initiated the development of a model that incorporates this process into the GEANT4 environment to facilitate the investigation and development of GSS with the use of easily available computing resources.

The simulation model has been developed in 2 parts – (I) Acquisition Geometry and Phantoms, and (II) Physics of NRF.

(I) **Acquisition Geometry and Phantoms**

The geometry of the GSS acquisition system in GEANT4 consists of three primary objects: World, Gamma Source, and Gamma Detectors. Each part has been designed as a separate Geant4 object to facilitate modifying individual parameters on one object independently of the others.

(a) **World:** Geant4 requires creation of a finite virtual space called the ‘world’, which acts as the world for the experiment. This world defines the virtual space within which the experiment will occur. All sources, detectors and samples are placed in the world. Particle interactions are tracked only as long as they occur in this world, and particles exiting the world are considered spent events. For the GSS system, the world has been defined as a geometric cube with edge 1m, and is filled with air.

(b) **Gamma Source:** The gamma source is created by defining a 'Geant4 Particle Gun', with user defined options for particle type and energy. While any combination of particle energy and type is possible, the GSS system uses gamma photons with energy equal to the energy state of interest in the element. For the excitation of natural iron, for example, the incoming particle energy is set to 846.7 keV and/or 3448 keV (both are discrete energy states in $^{56}$Fe). The gun also facilitates user-controlled beam widths of any dimension. The gamma source in this simulation produced a 1-cm wide gamma beam with energy precisely tuned to 846.7 keV or 3448 keV.

(c) **Gamma Detectors:** In the previous year, we had modeled two types of detectors in the simulation: Experimental gamma detectors, and a surface gamma detector. In the second year of the project, we expanded the utilities of both detector objects to evaluate new and advanced acquisition techniques. The original detector objects are described below in parts (i) and (ii), and the improvements are described in part (iii).

(i) **Experimental Gamma Detectors**: These detectors are created as solid cylinders with user-defined diameter and height. Each cylinder is filled with high-purity germanium, HPGe (density= 5.32 g/cm$^3$), corresponding to the material of the HPGe detectors used in the physical experiment. The detector material is 'sensitized', i.e. defined to track particle interactions and record the energy deposited at each interaction. The detector can be placed at any location in the world. In the current configuration, the detector is modeled as a 30-cm diameter cylinder with 10-cm height, similar to the detectors used in the physical GSS experiments. The detector is placed at an angle corresponding to maximum emission from the sample (which, in the case of 56-Fe at 846 keV, is at 90 and 270 degrees). An example of these detectors (green) is shown in Figure 5(a).

(ii) **Surface Gamma Detector:** This detector is modeled as a solid sphere that completely encloses the gamma-ray source and the target sample. The inner surface of the detector is sensitized to track a particular type of radiation, in this case, Gamma. Every gamma photon incident on the detector surface is reported as a 'hit'. The detector provides two advantages over the experimental HPGe detectors described above: (a) It allows detection of all particles emitted around the sample (i.e. 360-degree solid-angle detection), and (b) It facilitates monitoring of the emission pattern modeled into the simulation. The first criterion contributes significantly to improving the computing efficiency of the model, as the detector is able to utilize the information from every gamma particle emitted. Therefore, it is possible to analyze the working of the simulation using a significantly smaller number of incident particles, which improves the computing efficiency. The second criterion provides an error-checking mechanism to constantly monitor and evaluate the behavior of the simulation physics. Because we are developing a previously unexplored feature into the GEANT4 model, it is imperative to perform continuous and careful monitoring of the model behavior to ensure that the simulated results are a close match to the physical world. The surface detector facilitates such monitoring through a convenient and efficient manner. The surface detector is shown in Figure 5(b).

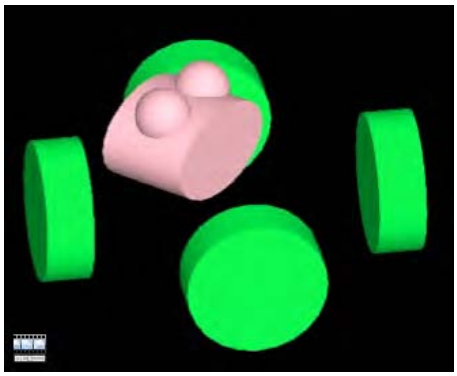

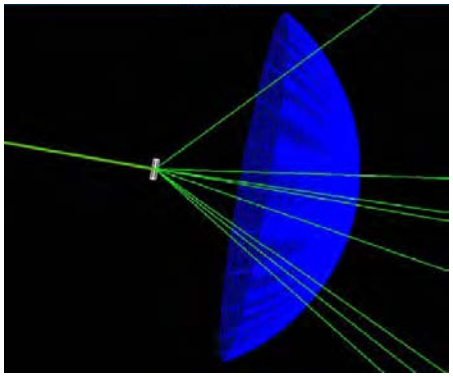

**Fig. 5. (a)** An example of the geometry with the world housing the detector and the breast phantom. The target gantry is an invisible box around the phantom. The gun is an invisible source at the left edge of the figure. The detectors are modeled as solid cylinders of pure germanium (HPGe), shown in green. **(b)** A simulated run using the hemispherical surface detector (shown in blue). The gun emits gamma particles from the left-most edge of the figure (particle path shown in green). The gamma photons interact with the sample and produce nuclear resonance gamma radiation. The energy and position of incidence of the emitted gamma-rays is recorded by the surface detector.

(iii) **Improvements in detector systems:** Over the last year, three new features have been added to the detectors to improve system sensitivity and detection efficiency. The features are as follows:

**a. Voxelization:** Using the GEANT4 parameterization function, the gamma ray detectors and samples have been converted into voxelized volumes to enable tracking energy deposits within different parts of the volume. Through GEANT4's parameterized tracker, each individual voxel of the volume can be made to track deposited energy, which facilitates visualization and measurement of the energy deposited within the volume. Figure 6(a) shows an example of a segmented volume and Figures 6(b) and 6(c) show reconstructed images of the energy deposit within a voxelized breast tissue phantom. The beam enters from the lower edge of the cube (red parts indicating higher energy deposits) and penetrates upwards (blue parts indicating lower energy deposit). From this figure, it is evident that the energy deposit outside the beam plane is considerable lower than in the beam path (as expected). This data will be used to determine the optimal shape and size of the gamma-ray detector, to evaluate the beam requirements for irradiation of specific breast shapes, and to accurately measure gamma radiation dose for patients of various shapes and sizes.

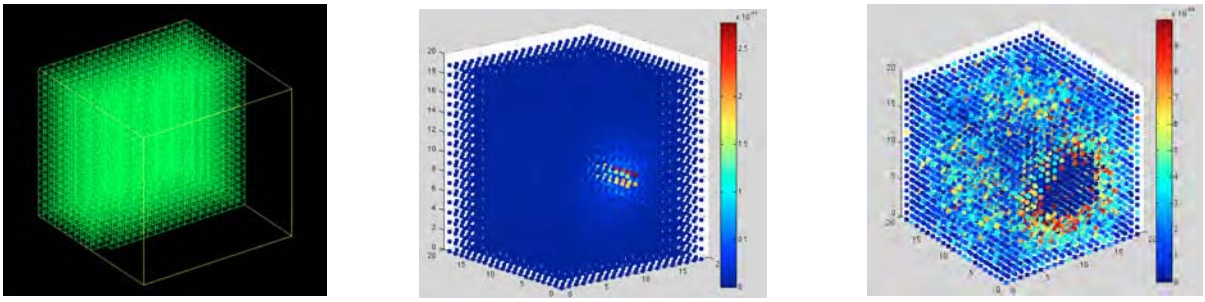

**Fig. 6. (a)** An example of a voxelized sample in GEANT4. The sample in this example is a cube containing breast tissue (shown partially voxelized). Each voxel measures 1 $mm^3$ in volume. **(b)** A quantitative map of the highest energy deposited in the voxelized cube phantom. Energy tracking is performed within each individual voxel of the cube. In this figure, the beam enters through the right part of the cube (shown in red, corresponding to highest energy deposit) and exits towards the left back edge (shown in blue corresponding to lower energy deposit). **(c)** The energy deposited in the remaining part of the cube (outside the central high-energy region). This figure demonstrates the ability to track energy within each individual section of the detector or sample volume. (Note: See figures

**b. Coordinate tracking – surface detector:** The default surface detector included in GEANT4 limits the tracking ability to one dimension; i.e., it divides the detector surface into a set number of slices in any one dimension and sums the energy deposited for each slice. Although this ability is useful, it limits functionality of the detector when two-dimensional emission patterns need to be imaged. To include this feature, we developed a completely new analytical model of the surface detector, which is divided into pixels of user-defined size and reports the energy deposited at the detector surface in each pixel. Figure 7 shows examples of the emission patterns measured using the surface detector. The detector can be set to image a single energy transition [which is an important feature for GSS; Figure 7(c)] or track a wide energy range for other applications [such as in Figures 7(a) and 7(b)].

**c. Detector timing and tracking**: The new analytical surface detector has also been given the ability to track time of flight (TOF) to facilitate TOF gamma imaging. By tracking the flight time and arrival time of gamma photons at the detector surface, the detector can identify the position of the emitted gamma within the phantom. This capability of the detector is currently being refined to improve the precision of detection.

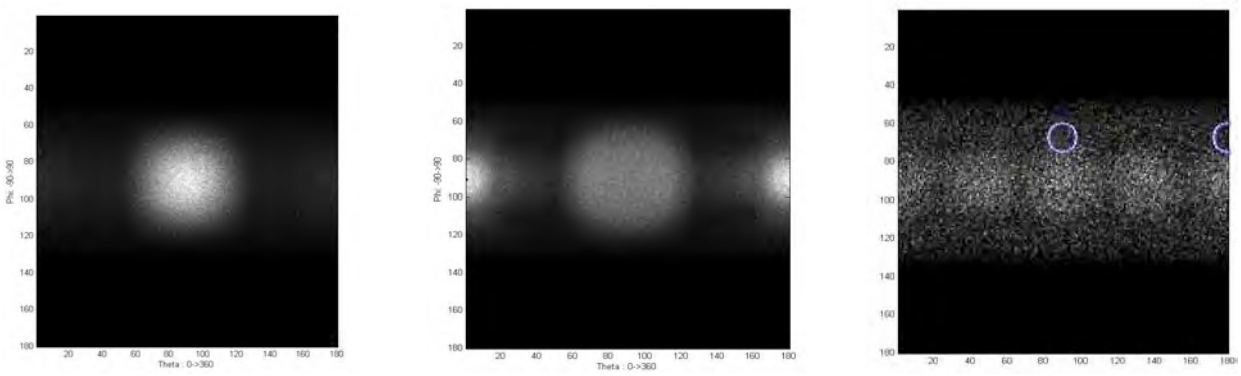

**Fig. 7.** Distributions of incident radiation measured by the pixelated surface detector. The detector reports the results in both polar and Cartesian coordinates for a predefined number of energies or energy ranges. **(a)** The energy of the incident beam (in this case neutrons) incident on breast tissue. Most of the beam intensity is centered along the beam path and is therefore incident at the center of the detector surface. **(b)** A thresholded energy map showing the scattered lobes of the incident beam particles. In addition to the primary lobe at the center, scattered lobes are visible at 90-degrees with respect to the beam direction. **(c)** The detected gamma distribution for a single filter set around 847 keV (i.e., $^{56}$Fe). The emission exhibits a quadrupole profile with 4 distinct lobes visible clearly. This information is used to identify the optimal location for positioning the HPGe gamma-ray detectors using a ratio of the highest emitted gamma intensity vs. lowest incoming gamma incidence.

**(d) Simulated phantoms:** Two sets of phantoms have been designed for use in this project – (a) Breast Phantom (b) Dose Phantom. Both phantoms have been developed earlier and are available for direct incorporation into the NRF simulation model in GEANT4. A description of the phantoms is provided here in the interest of making this report comprehensive in its description.

i. **Breast Phantom:** Breast phantoms are simulated in GEANT4 as ellipsoids of shape and size that matches the average human adult. An example of the phantom is shown in Figure 5(a). The phantom can be filled with benign or malignant breast tissue, which is classified on the basis of its elemental composition as shown in Table 1 below. Apart from the regular elements found in human breast tissue, i.e. hydrogen, oxygen, carbon and nitrogen, the breast tissue models are given trace elements in concentrations corresponding to benign and malignant breast tissue as reported in [2-6, 10]. The density of breast tissue was defined as 0.93 g/cm$^3$.

| | O | C | H | N | Cl | Na | K | Fe | Ca | Zn | Br | Al | Rb | Mn | Co | Cs |
|---|---|---|---|---|---|---|---|---|---|---|---|---|---|---|---|---|
| **Norm (%)** | 6.14 E+01 | 2.29 E+01 | 1.26 E+01 | 2.57 E+00 | 1.98 E-02 | 1.85 E-02 | 8.94 E-02 | 9.80 E-03 | 8.29 E-03 | 1.17 E-03 | 7.07 E-04 | 6.67 E-04 | 5.98 E-04 | 3.88 E-05 | 2.06 E-05 | 3.27 E-07 |
| **Malig (%)** | 6.14 E+01 | 2.29 E+01 | 1.25 E+01 | 2.57 E+00 | 2.15 E-02 | 2.00 E-02 | 1.96 E-02 | 7.85 E-03 | 1.13 E-02 | 1.14 E-03 | 6.55 E-04 | 5.70 E-04 | 5.84 E-04 | 3.16 E-05 | 1.98 E-05 | 3.60 E-07 |

Table 1: Breast tissue composition for normal and malignant models (from [11]).
The percentages were calculated by converting dry weights to wet weights.

ii. **Dose Phantom:** Three dosimetry phantoms have been modeled and used in this study. The first, which is included in GEANT4, is a whole body phantom that contains all major organs in the body including the breast. This phantom is made up of simply geometric approximations of each organ, and the user can define the material in the organ to match the properties of the tissue. The phantom tracks the energy deposited within each individual organ, which facilitates monitoring of the whole-body dose from a single GSS scan. The phantom is shown in Figure 8(a). The second dosimetry phantom focuses on the torso only (including the breasts and other major organ such as the lungs and heart) and accounts for the larger anatomic structures encountered by a gamma beam when scanning the patient. The torso is modeled as a large ellipsoid and the breasts are modeled as hemispheres that are connected to the torso. Both regions are filled with water to simulate scattering in tissue. The entire phantom is sensitized to measure the energy deposited

in the torso, and the results are reported individually for each organ and for each individual voxel in the breast. The cumulative energy deposit can then be converted to an absorbed-dose-equivalent to obtain an estimate of the whole-body and individual organ dose received through a GSS scan. The phantom is shown in Figure 8(b). The third phantom is the parameterized, voxelized breast model used to generate maps of radiation dose within different parts of the irradiated volume (shown in Figure 6b, 6c and 8c). Figure 9 shows the energy deposits in different parts of the voxelized breast model.

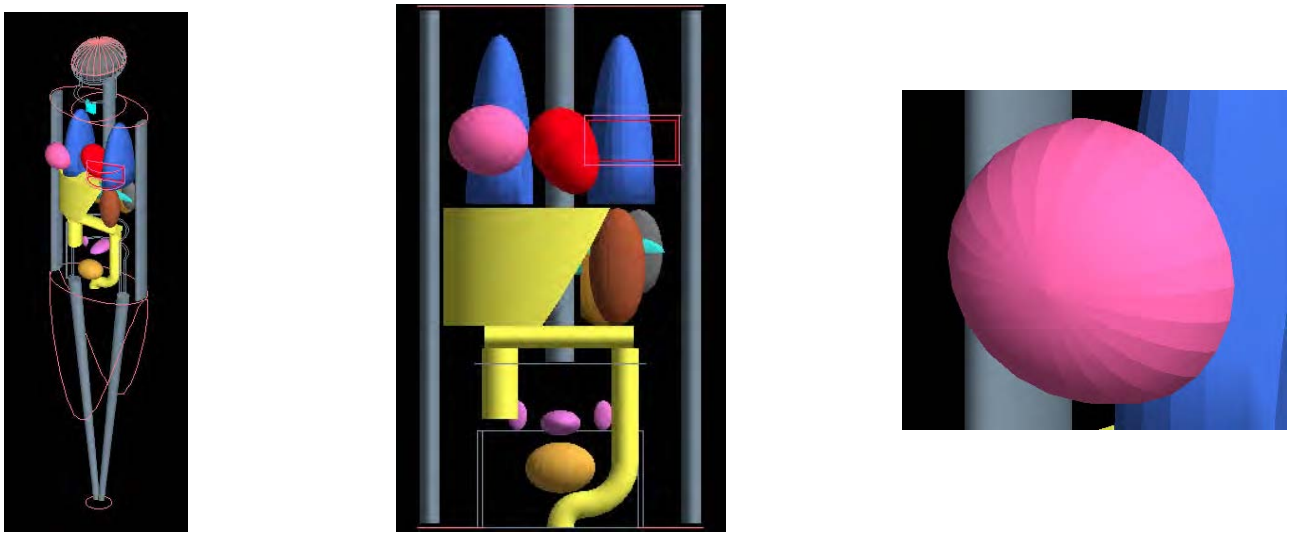

**Fig. 8.** Dosimetry phantoms in GEANT4 to measure radiation dose from a GSS exam. **(a)** The whole body phantom measures the dose deposited in each organ within the body. **(b)** The phantom includes the breast and most of the surrounding vital organs in the torso including the lungs, heart and thyroid. **(c)** The second phantom focuses on the breast and the closest vital organs such as the lungs and heart. The breast is parameterized so that energy is tracked within each section of the organ. The individual parameterized sections of the breast are visible in this image.

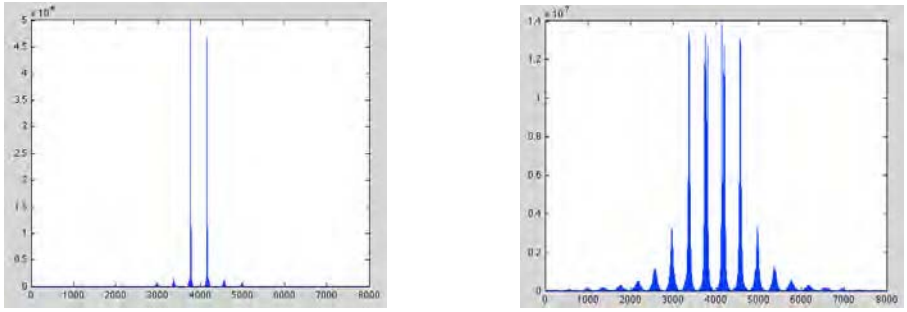

**Fig. 9.** Dosimetry tracking within the voxelized breast volume showing highest dose in the regions illuminated by the beam (which is expected). **(a)** The highest dose regions correspond to the two centrally located peaks. **(b)** The energy deposited in the remaining part of the liver (after the central peaks are truncated). The energy deposit reduces exponentially with increasing distance from the beam center. This data allows evaluation of the effect of different beam widths on the radiation dose encountered in the GSS scan.

## (II) **Modeling NRF Physics**

Nuclear Resonance Fluorescence (NRF) is a process that describes the resonant nuclear absorption of a photon followed by its de-excitation and subsequent emission of one or more gamma particles. Without taking Doppler Broadening into account, the cross section of the resonance follows a Breit-Wigner shape that can be described by the following equation:

$$\sigma(E)=\pi\left(\frac{\lambda}{2\pi}\right)^2\frac{2J_1+1}{2J_0+1}\frac{\Gamma_0(\Gamma/2)}{(E-E\gamma)^2+(\Gamma/2)^2}$$

where λ is the wavelength of the incident photon, *Er* is the resonance energy, *J*0 and *J*1are the nuclear spins of the corresponding ground state and excited state, respectively, Γ0 is the partial width to the ground state, and Γ is the total decay width of the excited state. For our interests, the resonance condition is satisfied if the incident energy of the gamma ray is equal to the resonance energy of nucleus. In this case, the nucleus gets excited and subsequently decays by re-emission of the radiation. Two energy states were used as a starting point for the development of the simulation physics: one at 846.776 keV (i.e., the first excited energy in natural iron) and the other at 3448 keV. The second energy level presents a more suitable option, both in terms of the resonance width and the energy range of the HIGS source. The NRF Process developed in this project comprises a set of C++ classes implemented through the following 3 steps:

(i) Coordinate extraction of relevant nuclear level data from from the Evaluated Nuclear Structure Data File database

(ii) Specify the probability of occurrence of the NRF process as a function of photon energy and the density of materials

(iii) Identify the final state and introduce the class in Geant4 to complete the decay of the excited nucleon.

Although both excitation and de-excitation proceed via the EM interaction, Geant4 treats them as Gamma-Nuclear interactions, which are a part of hadronic physics. Figure 10 shows an overview of the design of the NRF Process.

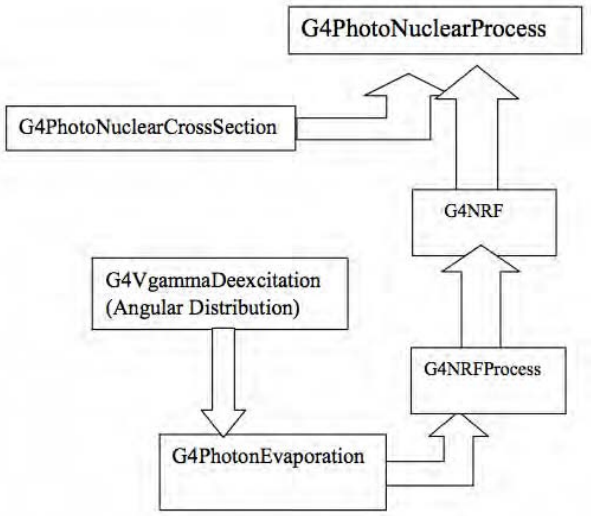


Figure 10. An overview of the GEANT4 NRF Physics design process.

The simulation code has been developed and preliminary testing has been performed using 2 criteria: (a) Angular distribution of emitted gamma particles, and (b) Emitted gamma energy distribution. The testing criteria and results have been described below.

**(a) Angular Distribution:** Gamma emission from nuclear energy transitions follows an angular distribution that is well known. In the case of the two states modeled here, the angular distribution follows dipole and quadrupole profiles for the 3448 keV and 846.77 keV states, respectively (as expected). The dipole emission profile shows local maxima at 0° and 180° with respect to the incoming gamma beam, while the quadrupole emission profile shows an additional local maximum at 90°. For the simulation to be valid, the emission profiles of the gamma particles emitted as a result of NRF must exhibit identical emission profiles as their theoretical counterparts.

The simulation was executed with a model of iron in water and emitted gamma counts were acquired using the 360° spherical surface detector (shown in Figure 3 and 4). The resulting spectra are shown in Figure 11. In both

cases, the emitted gamma profile showed maximum counts at 0° and 180° for the dipole emission profile, and 0°, 90° and 180° for the quadrupole profile. In the quadrupole emission profile, the peak at 90° was found to be smaller than the peaks at 0° and 180°. This behavior is consistent with the expected theoretical values.

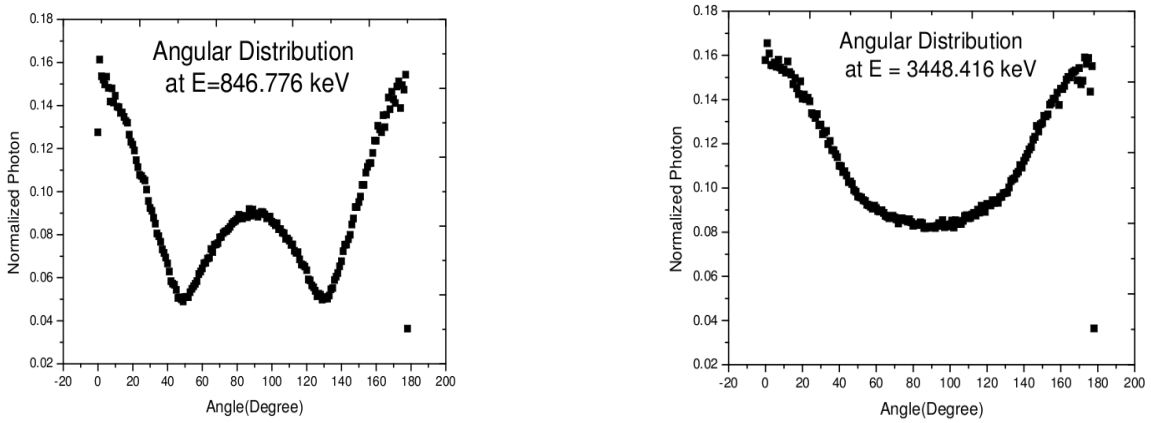


Figure 11. Angular emission profiles of the gamma particles emitted in the NRF simulations. Both profiles showed excellent agreement with the theoretical expected values. **(a)** The quadrupole emission profile for 846.77 keV showed local maxima at 0°, 90° and 180°. **(b)** The dipole emission profile for 3448 keV showed maxima at 0° and 180° only.

**(b) Energy Distribution:** The NRF process relies on the large difference between the interaction cross-section inside the resonance energy window and the cross-section outside the window. Therefore, if the resonance properties have been accurately modeled, the simulation must show very high interaction cross-section when the energy of the incoming gamma particle is within the resonance window of the nuclear energy state, and almost no interactions otherwise. The simulation was executed using the iron-water phantom and the surface detector, with both energies used for the incoming gamma particles. Figure 16 shows the output of the energy distribution of the emitted gamma particles for both energy states modeled.

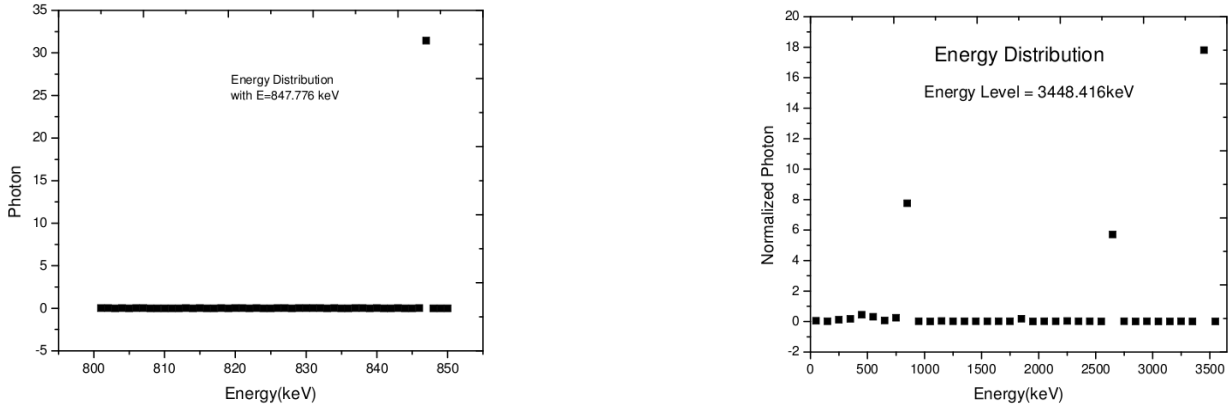


Figure 12. Energy profiles of the gamma particles emitted in the NRF simulations. Both profiles showed excellent agreement with the theoretical expected values. In each profile, the highest gamma yield was observed at the energy corresponding to the nuclear energy state of the element. In the case of the 3448 keV state, additional gamma lines were seen at 2601keV and 846.77 keV, which are due to the cascading of energy state transitions from the 3448 keV state.

In both cases (i.e., 846.77 keV and 3.448 MeV), gamma yields were obtained at the correct energies including the energies corresponding to cascaded levels. For example, the 3.448 MeV state decays to the ground state with the emission of a 3.448 MeV gamma particle. In addition, it may decay to the 846.77 keV state with the emission of a 2.601 MeV gamma particle. Therefore, when the 3.448 MeV state is stimulated, we observe high gamma yields at 3.448 MeV, 2.601 MeV and 846.77 keV. All of these phenomena were observed in the simulation.

(III) **Image Reconstruction**

Although image reconstruction was not a proposed part of the original project, we have added the ability in the simulation to acquire and generate reconstructed images of the elemental distribution. Due to the dose constraints of high-energy gamma beams, a GSS scan must reconstruct images of the scanned objects with minimal radiation to the patient. One of the techniques of minimizing dose is to use undersampled acquisition geometries (with very few angles) and overcome the sampling deficiency through an appropriate reconstruction algorithm. We have identified a suitable reconstruction algorithm and a preliminary acquisition geometry through our concurrent work with neutron detection systems. The Maximum Likelihood Expectation Maximization (MLEM) algorithm presents an excellent option for image reconstruction in GSS due to its high performance accuracy in undersampled systems. The MLEM implementation for PET and SPECT is easily adaptable to GSS due to the similarities in the physics of detection between these techniques. In all 3 techniques, the gamma rays to be imaged are emitted from within the sample in a 360º solid angle around the sample. The principles of gamma detection, albeit at different energies for the three techniques, exhibit considerable similarity in the physics processes governing the overall detection efficiency. Thus, MLEM represents an ideal reconstruction algorithm for image reconstruction in GSS.

Note: The NRF simulation in GEANT4 is still in its early stages; i.e., it has not yet been extensively validated and verified by the GEANT4 user community. Therefore, the development and testing of the image reconstruction algorithms has been performed with well-tested and validated neutron interactions in GEANT4. Although neutrons are used to stimulate the gamma emission, the stimulated nuclei exhibit identical behavior as in GSS; i.e., they emit the same characteristic gamma photons with the same emission profiles. Due to the extensive neutron validation and testing database available in the GEANT4 community, neutrons were chosen over gamma beams as the radiation source of choice at this stage of simulation development.

The breast phantom shown in Figure 5(a) was scanned using neutron beams translated through the sample. The breast phantom was modeled as a combination of an elliptical tube torso and hemi-spherical breasts. The torso measured 30 cm and 20 cm (major and minor axes, respectively) and 20 cm in height. The breasts measured 12 cm in diameter. Each breast was given a single tumor measuring 2 cm in diameter. The two tumors were given different trace element concentrations (shown in Table 1) to model the normal and malignant disease conditions. The torso was modeled as water to simulate the neutron-scattering properties of the human body. Fig. 13 shows the top view of the breasts with the enclosed lesions. The red lesion was made malignant and the blue lesion was normal tissue. Each breast was given the opposite material as its lesion. Tomography was performed by translating and rotating the phantom in the space between the HPGe detectors while keeping the source and detectors still, which is equivalent to the conventional tomographic process of moving the source and detectors simultaneously around a still phantom. The scanning was performed using a 5-MeV neutron beam with 5-mm beam width over 24 angles from 0-180 degrees.

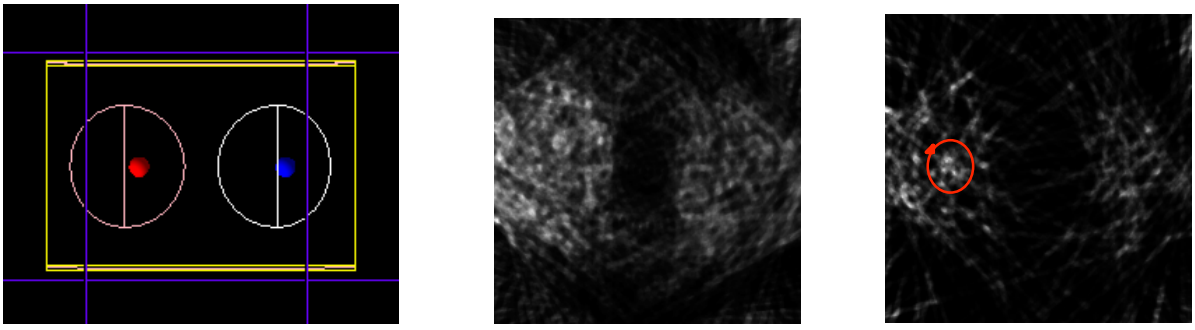

Fig.13. **(a)** Top view of the breast phantom showing the torso (yellow rectangular box), the two breasts (larger circular objects) and one lesion in each breast (smaller, solid spheres). The left breast (normal tissue) contains the red malignant lesion and the right breast (malignant tissue) contains the blue normal tissue lesion. The four solid purple lines mark the extreme positions of the neutron beam used in the tomographic acquisition, enclosing a square area between them that corresponds to the field of view of the reconstructed image. **(b)** Reconstructed image for $^{12}C$ at 4439 keV corresponding. The image shows the 3$^{rd}$ iteration of the MLEM algorithm. The location of carbon in the image matches perfectly with the region corresponding to the breast tissue. The right breast shows reduced intensity due to neutron attenuation (the beam entered the image from the left side). **(c)** Reconstructed

image for $^{23}Na$ ($3^{rd}$ iteration of the MLEM algorithm). The red circle denotes the location of the tumor in the left breast, which shows higher pixel intensity corresponding to an elevated elemental concentration in the malignant tissue.

Images were reconstructed for several elements associated with cancer (including Fe, Al, Cu, Br, Se, Rb and Zn). The reconstructed images showed excellent correlation between the location of the lesion and the increase in the concentration of the element. We are now working on generating similar images using the gamma source beams through the NRF interaction.

In this task, we have developed a preliminary working model of NRF in the GEANT4 simulation environment. In addition to the two energy levels in $^{56}Fe$ (a cancer-marking element), we are working on including all other prominent elements found in the body (i.e., carbon, hydrogen, oxygen and nitrogen), as well as cancer-marking trace elements such as gold, rubidium, antimony, cesium, selenium, iron, copper and zinc into the model. In addition, we have developed advanced simulated phantoms of the breast and gamma-ray detectors that will facilitate improvements in detection sensitivity and acquisition efficiency. The voxelized dosimetry models allow evaluating the effects of different GSS beam widths on the radiation dose delivered to each organ in the body, and the voxelized and surface detectors allow improvements in detection sensitivity through time-tagging of the detected gamma photons.

**Task 4: Determine efficacy of the complete system on detection and diagnosis of breast cancer with benign and malignant tissue specimens.** Months (30-36)

**Status:** Pending.

## KEY RESEARCH ACCOMPLISHMENTS

- A working prototype of the GSS acquisition system has been designed and assembled using the HIGS source at Duke University.
- The prototype system has been used to obtain spectral data from two important elements that are early indicators of breast cancer.
- A working Monte-Carlo simulation of the NRF process has been designed and implemented in the Geant4 environment, which makes it possible to continue system evaluation and development without requiring access to the HIGS beam.
- Two types of gamma detectors have been designed in the simulation environment with advanced capabilities that facilitate the evaluation of simulation performance in an efficient manner.
- Whole body and detailed organ dosimetry models have been designed in GEANT4 to evaluate the effect of GSS scanning on the human body.
- Phantoms for benign and malignant breast tissue populations have been designed and implemented in GEANT4. These phantoms are currently being used to generate data for training of a classifier algorithm.
- An artificial-intelligence classifier algorithm has been implemented to identify an optimal signature of cancer based on the detected elements.
- An image reconstruction technique was identified and implemented to generate tomographic images acquired through GSS (this was not a part of the original proposal; it represents an exciting new possibility for the proposed GSS technique).

## REPORTABLE OUTCOMES

The following conference proceedings and manuscripts have been generated through this project. Wherever available, a copy of the document has been attached in the appendix.

1. Agasthya GA and Kapadia AJ, “Locating stored iron in the liver through attenuation measurement in NSECT”, *Proceedings of IEEE Nuclear Science Symposium, Medical Imaging Conference*, pp. 2419-2422, 2009.

2. Kapadia AJ, Agasthya GA, Cumberbatch LC, Howell CR, “In-Vivo Iron Measurement Through Nuclear Resonance Fluorescence”, 52nd Annual Meeting of the American Association of Physicists in Medicine, Philadelphia, Pennsylvania, USA, 2010.

3. Kapadia AJ, Shah JP, Agasthya GA, “Quantitative Elemental Imaging with Neutrons for Breast Cancer Diagnosis: a GEANT4 Study”, *Proceedings of IEEE Nuclear Science Symposium, Medical Imaging Conference*, 2010.

4. Agasthya GA, Shah JP, Harrawood BP and Kapadia AJ, “Sensitivity analysis for liver iron measurement through neutron stimulated emission computed tomography”, *Physics in Medicine and Biology* (in review).

## CONCLUSION

We have developed a working prototype of the GSS acquisition system using the HIGS gamma source at Duke University. The working of the prototype device has been demonstrated using phantoms of iron and copper in water, both elements being potential markers of breast cancer. We have developed a simulation of the NRF process in GEANT4 (Monte Carlo simulation environment) and modeled a variety of breast cancer phantoms and gamma-ray detectors. We now focus on generating data from the simulation model to identifying the most suitable candidate elements for breast cancer diagnosis through GSS.

## REFERENCES


[1] ACS, "Cancer Facts and Figures 2007," American Cancer Society, Atlanta 2007 2007.

[2] Garg A, V. Singh, et al., "An elemental correlation study in cancerous and normal breast tissue with successive clinical stages by neutron activation analysis," *Biological Trace Element Research*, vol. 46, pp. 185-202, 1994.

[3] Mussalo-Rauhamaa H, Piepponen S, Lehto J, Kauppila R, and Auvinen O, "Cu, Zn, Se and Mg concentrations in breast fat of Finnish breast cancer patients and healthy controls," *Trace Elements in Medicine*, vol. 10, pp. 13-15, 1993.

[4] Ng K-H, Bradley D, and Looi L-M, "Elevated trace element concentrations in malignant breast tissues," *British Journal of Radiology*, vol. 70, pp. 375-382, 1997.

[5] Ng K-H, Ong S-H, Bradley DA, and Looi L-M, "Discriminant analysis of normal and malignant breast tissue based upon INAA investigation of elemental concentration," *Appl. Radiat. Isot.*, vol. 48, pp. 105-109, 1997.

[6] Rizk S and Sky-Peck H, "Comparison between concentrations of trace elements in normal and neoplastic human breast tissue," *Cancer Research*, vol. 44, pp. 5390-5394, 1984.

[7] Yaman M, Atici D, Bakirdere S, and Akdeniz I, "Comparison of trace metal concentrations in malign and benign human prostate," *J. Med. Chem.*, vol. 48, pp. 630-634, 2005.

[8] Floyd CE, Bender JE, Sharma AC, Kapadia AJ, Xia JQ, Harrawood BP, Tourassi GD, Lo JY, Crowell AS, and Howell CR, "Introduction to neutron stimulated emission computed tomography," *Physics in Medicine and Biology*, vol. 51, pp. 3375-3390, 2006.

[9] Floyd CE, Howell CR, Harrawood BP, Crowell AS, Kapadia AJ, Macri R, Xia JQ, Pedroni R, Bowsher J, Kiser MR, Tourassi GD, Tornow W, and Walter R, "Neutron Stimulated Emission Computed Tomography of Stable Isotopes," *Proceedings of SPIE Medical Imaging 2004*, vol. 5368, pp. 248-254.

[10] Schwartz A and Fink R, "Trace Elements in Normal and Malignant Human Breast Tissue," *Surgery*, vol. 76, pp. 325-329, 1974.
[11] Bender JE, Kapadia AJ, Sharma AC, Tourassi GD, Harrawood BP, and Floyd CE, "Breast cancer detection using Neutron Stimulated Emission Computed Tomography: prominent elements and dose requirements," *Medical Phyiscs*, (submitted), 2007.
[12] Floyd CE, Kapadia AJ, Bender JE, Sharma AC, Xia JQ, Harrawood BP, Tourassi GD, Lo JY, Crowell AS, and Howell CR, "Neutron Stimulated Emission Computed Tomography of a Multi-Element Phantom," *IEEE Trans Med Imag (submitted)*, 2006.

**APPENDICES**

# Locating stored iron in the liver through attenuation measurement in NSECT

Greeshma A. Agasthya and Anuj J.Kapadia

*Abstract*– **Neutron stimulated emission computed tomography (NSECT) is a quantitative spectroscopic technique to detect element concentrations in the body. In previous work, we have demonstrated the ability to detect non-uniform distributions of iron overload in liver (in hemochromatosis) with a sensitivity of approximately 5mg/g. The diagnosis of hemochromatosis is performed by detecting characteristic gamma photons emitted by iron nuclei after they undergo inelastic scatter with incident neutrons. The efficiency of detection of the gamma photons is a combination of the attenuation of neutrons passing through the body and the attenuation of gamma photons before reaching the detectors. With non-uniform iron distributions, therefore, the resulting total attenuation depends on the position of the iron store within the body with respect to the neutron beam and the gamma detectors. We are developing an attenuation correction technique which takes into consideration the position of the iron-store in the liver to compute a correction factor based on a combination of neutron and gamma attenuation. In this work we present results from a Monte-Carlo simulation study exploring the effect of the location of the iron-store within the liver. The NSECT scanning geometry used for data collection was simulated in GEANT4 [1]. A lesion of iron was placed at different locations within the liver and scanned to obtain an estimate of the detected signal. An estimate of the unattenuated signal was obtained and used to determine the total attenuation in the liver tissue. The attenuation profile was obtained for each position of the lesion and compared against a theoretical value. The results were found to be in agreement with each other, indicating that a theoretically calculated attenuation profile can be accurately used to create attenuation maps and hence locate iron-stores in the liver using NSECT.**

## I. Introduction

LIVER iron overload (hemochromatosis) is a condition in which the liver stores excess iron in the body, often leading to tissue damage, cirrhosis, cardiac failure and hepatocellular carcinoma [7]. It has been shown experimentally that detection of liver iron overload through neutron spectroscopy techniques such as Neutron stimulated emission computed tomography (NSECT) can be performed as a non-invasive alternative to biopsy [2]. In NSECT, neutrons incident on the tissue undergo inelastic scattering with atomic nuclei, forcing them to emit gamma rays. The energy of the emitted gamma ray depends on the properties of the interacting nuclei, and is well-known and unique for most isotopes. In this application we look for the gamma-line at 846 keV corresponding to natural iron $^{56}$Fe. The goal of this project is to develop neutron and gamma attenuation look up maps dependent on the position of the stored liver-iron, which can be used to locate iron stores from real NSECT projection data.

Manuscript received Nov 13, 2009. This research was supported in part by the Department of Defense Breast Cancer Research Program under Grant W81XWH-09-1-0066, and in part by funds from the Department of Chemistry at Duke University.

Greeshma A.Agasthya is with the Department of Biomedical Engineering and Carl E Ravin Advanced Imaging Laboratories, Duke University, Durham, NC 27705, USA (telephone: 919-684-1468, e-mail: greeshma.agasthya@duke.edu).

Anuj J Kapadia is with the Department of Radiology and Carl E Ravin Advanced Imaging Laboratories, Duke University, Durham, NC 27705, USA (telephone: 919-684-1442, e-mail: anuj.kapadia@duke.edu).

## II. Motivation

While attenuation correction in emission computed tomography is a well known subject, such an experiment has not been performed for neutrons. The simulated data obtained is expected to reinforce the theoretical findings, thereby facilitating the use of attenuation profiles for attenuation correction in order to improve the sensitivity of the entire system. This project aims at creating an attenuation profile map based on the position of the stored liver-iron, which may be used to determine the location of the lesion along a projection in the liver through comparison of the measured and expected attenuation profiles.

## III. Methods

### A. Monte Carlo Simulation

A Monte-Carlo simulation of the NSECT acquisition system was set up in GEANT4 as shown in Fig. 1. [5]. The simulated system was based on the experimental acquisition system described in [6].

**Neutron source:** The neutron source was set to emit a mono-energetic beam of 5 MeV neutrons. The beam profile was square and set to 0.64 cm$^2$.

**Gamma-ray Detectors:** Six cylinders of germanium were used as gamma-ray detectors. Each detector dimension was set to 10 cm diameter and 10 cm height. Detectors were placed at +45 and –45 degree with respect to the center of the liver phantom on either side of the neutron beam. All six detectors in this model were placed at a backward angle with respect to direction of the beam. Density of the germanium detectors was 5.32 g/cm$^3$.

**Liver Phantom:** The liver phantom was modeled as a cube of side 15 cm simulating the composition and attenuation properties of liver tissue. A lesion of diameter 2 cm was used to model an iron concentration of 150 mg/g with liver composition as shown in table I.

To investigate the effect of lesion location on the observed attenuation profile, the lesion was moved in successive steps along the direction of the beam within the liver volume. The

first location (shown in Fig.1.) was at the edge of the liver cube. Each successive position was 2 cm farther from the edge of the liver along the direction of the neutron beam (shown in Fig. 2). The consecutive positions did not overlap. The gamma energy spectrum was collected at each of these positions with a scan of 2.5 million neutron events. A typical energy spectrum contains peaks from $^{56}$Fe, $^{12}$C, $^{72}$Ge, $^{14}$N and a neutron capture peak from $^{1}$H. The peak of interest $^{56}$Fe and its background peaks are shown in Fig. 3.

### B. *Attenuation Calculation*

For each position, the neutron attenuation (due to the liver material encountered by the beam up till the lesion) (table II) and gamma attenuation (due to the liver material between the lesion and detectors) (table III) were calculated as explained below in Section IV. The total attenuation is the product of the two calculated attenuation values (table IV). Each combination of lesion position and detector has a calculated attenuation value: [exp(-Mu*t)].

Data were also obtained from a simulated lesion at each of the lesion positions but without the surrounding liver tissue. These counts ($I_0$) were used to obtain an estimate of the signal loss due to detector effects (i.e. detector material efficiency, position and detector solid angle efficiency). The gamma counts obtained with the surrounding liver tissue were corrected for background to reduce the effects such as Compton Scattering and contributions from elements other than iron [8]. The background corrected counts (I) gave an estimate of the gamma counts detected with attenuation. Total observed attenuation was calculated as the ratio of the two measured values [$I/I_0$]. Therefore, the resulting measured attenuation value represented the attenuation observed due to the liver tissue alone.

## IV. MATH

The neutron attenuation coefficient of the composition of liver was calculated by multiplying the mass of individual elements with their respective neutron absorption cross-sections to obtain the neutron attenuation co-efficient of individual elements. The elemental composition of liver is shown in table I [3]. The sum of elemental neutron attenuation coefficients was used to obtain the neutron-attenuation coefficient of the liver ($Mu_1$= 0.1406/cm). The gamma attenuation coefficient of water was used as an approximate value of gamma attenuation co-efficient of liver ($Mu_2$=0.0303/cm).

The Beer-Lambert attenuation formula was used to obtain calculated attenuation values for comparative studies. The formula is:

$$\mathbf{I/I_0 = exp(-Mu*t)}$$

where,

$Mu*t = Mu_1*t_1 + Mu_2*t_2$

$Mu_1$: Neutron attenuation coefficient ($cm^{-1}$)

$Mu_2$: Gamma attenuation coefficient ($cm^{-1}$)

$t_1$: Distance from liver edge to lesion center in the path of the neutron beam. (cm)

$t_2$: Path length in the liver of gamma photon traveling from the lesion to a detector. (cm)

$I_0$: Gamma counts from iron lesions without surrounding liver material.

I: Gamma counts from iron lesions with surrounding liver material.

## V. RESULTS

### A. *Figures*

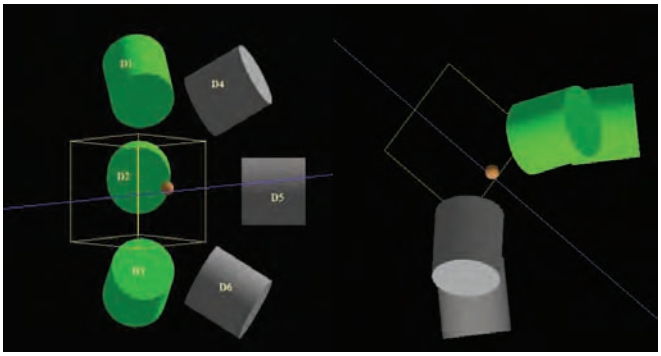


Fig. 1. A GEANT4 simulation of the experiment showing the side and top view of the setup. The liver phantom is shown as a cube (yellow), and the iron lesion is shown as a sphere (brown). The green and gray cylinders are the gamma detectors located at 45 degrees with respect to the center of the liver phantom on either side of the neutron source. D1, D2, D3, D4, D5 and D6 give the naming convention of the detectors. The blue line represents the neutron beam which originates from the same side as the detectors.

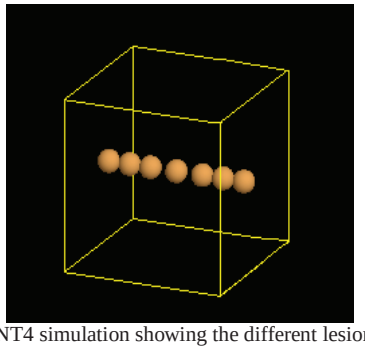

Fig. 2. The GEANT4 simulation showing the different lesion positions used.

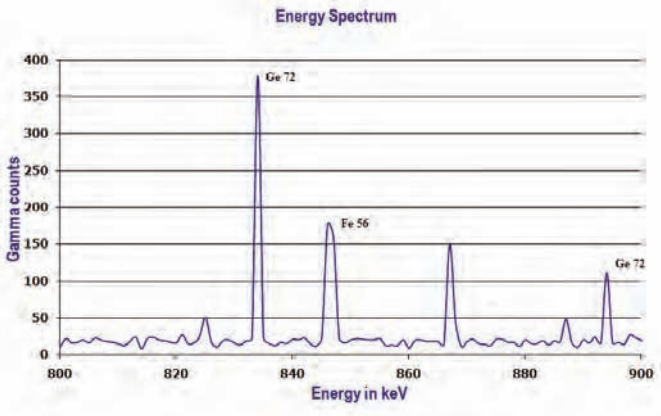


Fig. 3. Spectrum corresponding to the lesion at position P1 showing the $^{56}$Fe peak at 846 keV.

Fig.4. shows the number of gamma-rays detected at each lesion position with 2,500,000 incident neutrons through the Monte-Carlo simulation in GEANT4.

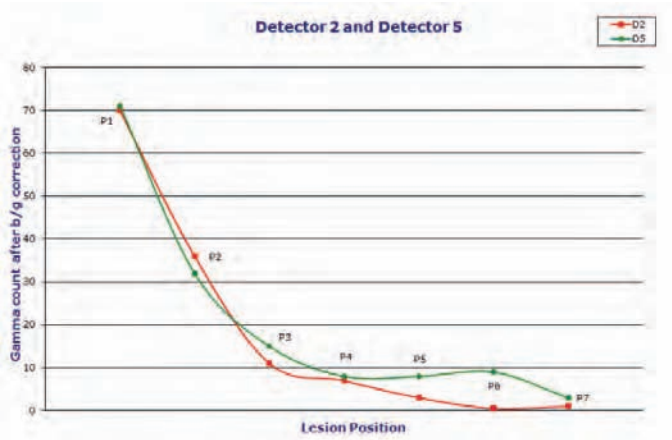


Fig.4. Number of gamma-rays detected by the center detectors (D2 and D5) [Fig. 1] at 846keV (energy corresponding to iron) are shown for different positions with P1 being the position closest to the detector and P7 being the farthest. Each successive position is separated by 2 cm. The gamma counts have been corrected for background effects.

Table II shows the calculation of neutron attenuation and gamma attenuation values for all lesion positions for detectors D2 and D5. Similar values are calculated for detectors D1, D3, D4 and D6. Fig. 5 shows the expected total attenuation calculated theoretically as a product of the gamma attenuation and neutron attenuation at each position of the lesion for each of the six detectors. Since detector D2 and D5 are placed symmetrically around the center of the liver in the plane of the lesion and neutron gun, they have the same attenuation profiles. Similarly D1, D3, D4 and D6 detectors are symmetric about the center of the liver and have the same attenuation profiles.

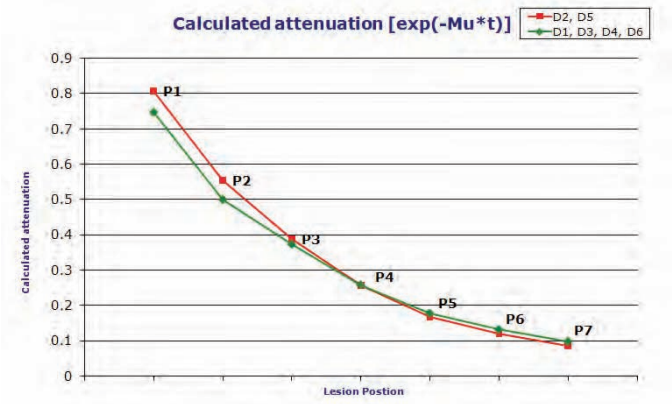


Fig.5.The product of the neutron attenuation and gamma attenuation are shown for different positions with P1 being the position closest to the detector and P7 being the farthest. The total attenuation calculated for D2 and D5 detectors (red) are equal as they are symmetrically placed. Similarly, calculated total attenuation for D1, D3, D4 and D6 detectors (green) are equal.

From fig.5 we see that the attenuation profiles for all detectors placed symmetrically about a certain point in the liver are equal for a given position. For further analysis we will use the data from detectors D2 and D5 to represent the entire data set.

Fig. 6 shows the comparison between the calculated and measured attenuation values. The measured value was taken as the average of the measured values obtained from detectors D2 and D5 for each lesion position. This information can be used to determine the position of the lesion along this particular projection.

For example, for the data shown in Fig. 6:

The calculated attenuation value at position P1 = 0.81.

The calculated attenuation value at position P2 = 0.55.

The measured attenuation value at position P1 = 0.74.

Now, as 0.81 < 0.74 < 0.55, from this observation we can predict that the lesion with a measured attenuation value of 0.74 lies between P1 and P2. This observation is true as all distance measurements are taken with respect to the center of the lesions, each lesion is 2 cm in diameter and centers of two consecutive lesions are 2 cm apart. Hence, half of the lesion at P1 lies between P1 and P2. This is also part of the lesion that directly sees the neutron beam.

Similar trends are observed (in fig. 6) for all the other lesion positions. Table V shows the absolute difference between calculated and measured attenuation values for each detector at each lesion position.

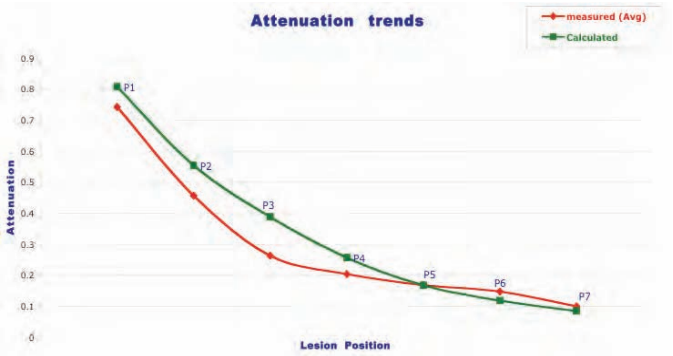


Fig. 6. Comparison between the calculated attenuation values (Green) and measured attenuation values (Red) for Detectors D2 and D5.

## B. *Tables*

TABLE I. ELEMENTAL COMPOSITION OF LIVER [4]

| Element | % by mass in Liver |
|---|---|
| Hydrogen | 10.2 |
| Carbon | 13.9 |
| Nitrogen | 3.0 |
| Oxygen | 71.6 |
| Sodium | 0.2 |
| Potassium | 0.3 |
| Sulphur | 0.3 |
| Chlorine | 0.2 |
| Phosphorus | 0.2 |
| Iron | 0.0 |

TABLE II. NEUTRON ABSORPTION CALCULATION

| Lesion Position | Mu per cm | t in cm | I/Io (neutron) |
|---|---|---|---|
| P1 | 0.14 | 1.00 | 0.87 |
| P2 | 0.14 | 3.00 | 0.65 |
| P3 | 0.14 | 5.00 | 0.49 |
| P4 | 0.14 | 7.50 | 0.35 |
| P5 | 0.14 | 10.00 | 0.24 |
| P6 | 0.14 | 12.00 | 0.18 |
| P7 | 0.14 | 14.00 | 0.14 |

TABLE III. GAMMA ATTENUATION CALCULATION

| Lesion Position | Mu per cm | t in cm | I/Io (Gamma) |
|---|---|---|---|
| P1 | 0.03 | 2.54 | 0.93 |
| P2 | 0.03 | 5.77 | 0.85 |
| P3 | 0.03 | 8.31 | 0.79 |
| P4 | 0.03 | 10.38 | 0.74 |
| P5 | 0.03 | 12.92 | 0.69 |
| P6 | 0.03 | 15.00 | 0.65 |
| P7 | 0.03 | 16.62 | 0.62 |

TABLE IV. TOTAL ATTENUATION CALCULATION

| Lesion Position | I/Io (neutron) | I/Io (Gamma) | Total Intensity |
|---|---|---|---|
| P1 | 0.87 | 0.93 | 0.81 |
| P2 | 0.65 | 0.85 | 0.55 |
| P3 | 0.49 | 0.79 | 0.39 |
| P4 | 0.35 | 0.74 | 0.26 |
| P5 | 0.24 | 0.69 | 0.17 |
| P6 | 0.18 | 0.65 | 0.12 |
| P7 | 0.14 | 0.62 | 0.09 |

TABLE V. ABSOLUTE DIFFERENCE BETWEEN CALCULATED AND MEASURED ATTENUATION VALUES

| Lesion Position | D1 | D2 | D3 | D4 | D5 | D6 |
|---|---|---|---|---|---|---|
| P1 | 0.05 | 0.22 | 0.32 | 0.20 | 0.13 | 0.07 |
| P2 | 0.11 | 0.05 | 0.15 | 0.02 | 0.08 | 0.22 |
| P3 | 0.09 | 0.15 | 0.08 | 0.18 | 0.16 | 0.02 |
| P4 | 0.06 | 0.12 | 0.05 | 0.13 | 0.08 | 0.12 |
| P5 | 0.09 | 0.09 | 0.04 | 0.06 | 0.01 | 0.07 |
| P6 | 0.05 | 0.10 | 0.01 | 0.01 | 0.20 | 0.07 |
| P7 | 0.10 | 0.05 | 0.24 | 0.06 | 0.01 | 0.10 |

### *C. Conclusions and Future work*

The results obtained show that there is a good match between the calculated and measured attenuation values for each detectors. Therefore, the calculated attenuation profile can be used to generate look-up maps that correspond to the location of the lesion along that projection. This information may then be used to identify the position of the lesion in the body. We are currently working on developing these prediction models using this detector set up with a better model of the anatomy of the liver. Further, this study will also be expanded to incorporate the effects of different iron concentrations into the predictor models. This technique of locating a lesion can be used to reduce dose to the patient as it reduces the number of projections required to scan an object.

## ACKNOWLEDGMENT

We thank Brian Harrawood at Carl E. Ravin Advanced Imaging Laboratories for his help with GEANT4.

## REFERENCES

[1] Kapadia AJ, Harrawood BP, Tourassi GD, “GEANT4 simulation of NSECT for detection of iron overload in the liver,” *Proceedings of SPIE Medical Imaging*, vol. 6913, pp. 691309, 2008.

[2] Kapadia AJ, Harrawood BP, Tourassi GD, “ A Geant4 Simulation for Iron Overload Detection using NSECT,” *Proceedings of IEEE Nuclear Science Symposium, Medical Imaging Conference*, vol. 6, pp 4604-4607, 2007.

[3] A. J. Kapadia and C. E. Floyd, "An attenuation correction technique to correct for neutron and gamma attenuation in the reconstructed image of a neutron stimulated emission computed tomography (NSECT) system," in *SPIE Symposium on Medical Imaging*, San Diego, CA, 2005, pp. 737-743.

[4] ICRU Report 46.

[5] V. N. Ivanchenko, "Geant4 toolkit for simulation of HEP experiments," *Nuclear Instruments and Methods in Physics Research Section A*, vol. 502, pp. 666-668 2003.

[6] S. Agostinelli, et. al., "GEANT4: A Simulation Toolkit," *Nuclear Instruments and Methods in Physics Research NIM A*, vol. 506, pp. 250-303, 2003.

[7] National Digestive Diseases Information Clearinghouse (NDDIC) “Hemochromatosis”, http://digestive.niddk.nih.gov/ddiseases/pubs/hemochromatosis/index.htm

[8] C. E. Floyd Jr., A. C. Sharma, J. E. Bender, A.J. Kapadia, J.Q. Xia, B. P. Harrawood, G.D. Tourassi, J.Y.Lo, M.R. Kiser, A.S. Crowell, R.S. Pedroni, R.A. Macri, S. Tajima, C.R. Howell, “Neutron stimulated emission computed tomography: Background corrections”, *Nuclear Instruments and Methods in Physics Research Section B: Beam Interactions with Materials and Atoms* Volume 254, Issue 2, January 2007, Pages 329-336

# Quantitative Elemental Imaging with Neutrons for Breast Cancer Diagnosis: a GEANT4 Study

Anuj J. Kapadia, Jainil P. Shah, Greeshma A. Agasthya

***Abstract*– Neutron stimulated emission computed tomography (NSECT) has been proposed as an early cancer-detection technique with the capability of 3-D tomographic imaging for identification of malignant tumors. In previous work we have demonstrated the ability of the technique to differentiate between normal and malignant breast tumors based on the concentration of cancer-marking elements in the tissue. Here we present tomographic images from a breast phantom with benign and malignant tumors simulated in GEANT4. A simulated model of the NSECT system was developed in GEANT4, along with phantoms corresponding to the human breast with benign and malignant tumors. Each tumor within the breast was given a different concentration of cancer-marking trace elements based on values reported in literature. The phantom was scanned with a 5-MeV neutron beam over a 180-degree angle. Tomographic images were reconstructed for six elements of interest from 10 different spectral lines. The results showed excellent agreement between the location of the tumor and the concentration of trace element detected in gamma lines from bromine, cesium, sodium and zinc. These results demonstrate the ability of NSECT in quantitative elemental imaging for breast cancer detection.**

## I. Introduction

NEUTRON Stimulated Emission Computed Tomography (NSECT) has been proposed as a novel method of detecting cancer in the body [1-4]. The technique is based on a unique trace-elemental signature of the malignant tissue, which can be used to differentiate between normal, benign and malignant tumors. NSECT uses inelastic scattering interactions between fast neutrons and naturally occurring cancer-marking elemental nuclei in the body to stimulate characteristic gamma emission from the nuclei. A gamma-ray spectrometer is used to generate a spectrum corresponding to the quantitative elemental profile of the scanned tissue. In previous work [3], we have described the use of the NSECT technique for the detection and classification of normal and malignant tissue in the breast based on the concentrations of several trace elements reported in literature, including Al, Br, Ca, Cl, Co, Cs, Fe, K, Mn, Na, Rb and Zn [5-11]. In the previous study, two elements, Br and Rb, were found to be particularly promising for differentiating between normal and malignant tissue [3].

Trace element variations are one of the earliest precursors of malignancy. Therefore, a technique capable of quantifying the concentrations of these elements may considerably enhance the early detection of the disease. Given the low concentrations of these elements in the body (typically a few micrograms of element per gram of tissue), their detection and accurate quantification is a considerable engineering challenge. In this project, we investigate the ability of the NSECT technique in detecting and classifying breast tumors through reconstructed images of trace element signatures.

## II. Method

All of the simulation models were developed using the GEANT4 toolkit [12, 13], version 9.3. GEANT4 provides an efficient virtual environment to model the high-energy physics interactions between particles and matter over a wide range of energies. It provides several powerful tools for developing radiation sources, detectors, and a variety of complex, anthropomorphic shapes corresponding to the human body. It permits the relative positioning and movement of each individual object with respect to another to facilitate tomographic acquisition.

The simulated model was designed in 3 parts – (a) Neutron Source, (b) Gamma-ray detectors, and (c) Breast phantom. Fig 1 shows a schematic of the simulated model with the three components. Each of these components is described below.

### *A. Neutron Source*

The neutron source was modeled as a GEANT4 general particle source (GPS) emitting 5-MeV neutrons in a 5-mm wide beam. The energy distribution of the neutron beam was monochromatic. The neutron fluence was controlled by specifying the number of neutron histories to be executed by the model.

Manuscript received November 21, 2010. This work was supported by the Department of Defense (Breast Cancer Research Program) under award number W81XWH-06-1-0484 and with funds from the Center for Molecular and Biomolecular Imaging at Duke University.

A. J. Kapadia is with the Department of Radiology and the Medical Physics Graduate Program, Duke University, Durham, NC, USA (phone: 919-684-1442; fax: 919-684-1491; email: anuj.kapadia@duke.edu).

J. P. Shah is with the Department of Biomedical Engineering and the Department of Radiology, Duke University (email: jainil.shah@duke.edu).

G. A. Agasthya is with the Department of Biomedical Engineering and the Dept. of Radiology, Duke University (email: greeshma.agasthya@duke.edu).

### B. *Gamma-ray Detectors*

The gamma-ray detectors were modeled as high-purity germanium (HPGe) (density= 5.32 g/cm$^3$) in one of two configurations: (a) Four cylinders of 30-cm diameter and 10-cm thickness (Fig.1), and (b) a 10-cm thick sphere surrounding the breast phantom (figure not shown). In the first configuration, the detectors were placed at angles of 45 and 135 degrees with respect to the beam, corresponding to the angles of maximum emission in several breast-cancer elements. In the second configuration, an oversized detector sphere was used to enhance gamma detection efficiency by subtending a larger surface area for detection. No additional shielding material was used in either configuration. The events recorded in the detectors were binned in 1-keV intervals, which is typical of a high-purity germanium detector (i.e. 0.1% energy resolution at 1 MeV).

### C. *Breast Phantom*

The breast phantom was modeled as a combination of an elliptical tube torso and hemi-spherical breasts. The torso measured 30 cm and 20 cm (major and minor axes, respectively) and 20 cm in height. The breasts measured 12 cm in diameter. Each breast was given a single tumor measuring 2 cm in diameter. The two tumors were given different trace element concentrations (shown in Table 1) to model the normal and malignant disease conditions. The torso was modeled as water to simulate the neutron-scattering properties of the human body. Fig. 1 shows an orthogonal view of the breast phantom, and Fig. 2 shows the top view of the breasts with the enclosed lesions. The red lesion was made malignant and the blue lesion was normal tissue. Each breast was given the opposite material as its lesion.

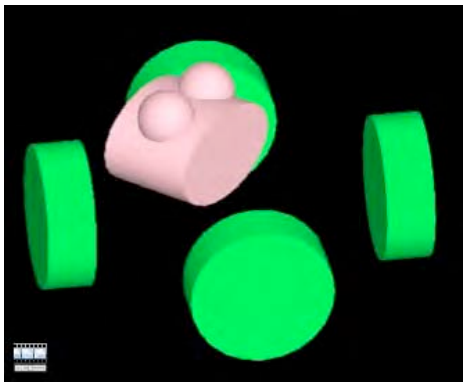

Fig.1. GEANT4 simulation of the NSECT system showing the breast phantom (pink) surrounded by four HPGe detectors (green). The neutron source is not visible in this image. The phantom was translated and rotated in the space between the detectors to facilitate tomographic acquisition.

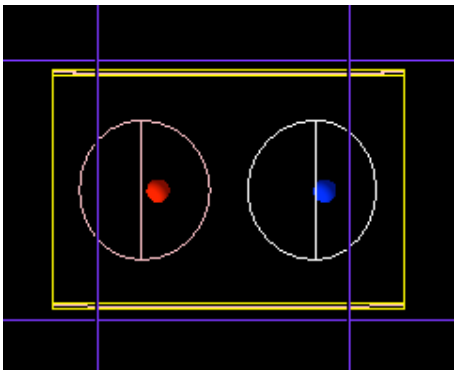

Fig.2. Top view of the breast phantom showing the torso (yellow rectangular box), the two breasts (larger circular objects) and one lesion in each breast (smaller, solid spheres). The left breast (normal tissue) contains the red malignant lesion and the right breast (malignant tissue) contains the blue normal tissue lesion. The four solid purple lines mark the extreme positions of the neutron beam used in the tomographic acquisition, enclosing a square area between them that corresponds to the field of view of the reconstructed image.

Tomography was performed by translating and rotating the phantom in the space between the HPGe detectors while keeping the source and detectors still, which is equivalent to the conventional tomographic process of moving the source and detectors simultaneously around a still phantom. The scanning was performed using a 5-MeV neutron beam with 5-mm beam width over 24 angles from 0-180 degrees.

TABLE I
ELEMENTAL COMPOSITION OF THE BREAST PHANTOM (FROM [3] ).

| Element | Normal (%) | Malignant (%) |
|---|---|---|
| O | 61.43 | 61.43 |
| C | 22.86 | 22.86 |
| H | 12.65 | 12.51 |
| N | 2.57 | 2.57 |
| Cl | 1.98 E-2 | 2.15 E-2 |
| Na | 1.85 E-2 | 2.00 E-2 |
| K | 8.94 E-2 | 1.96 E-2 |
| Fe | 9.80 E-3 | 7.85 E-3 |
| Ca | 8.29 E-3 | 1.13 E-2 |
| Zn | 1.17 E-3 | 1.14 E-3 |
| Br | 7.07 E-4 | 6.55 E-4 |
| Al | 6.67 E-4 | 5.70 E-4 |
| Rb | 5.98 E-4 | 5.84 E-4 |
| Mn | 3.88 E-5 | 3.16 E-5 |
| Co | 2.06 E-5 | 1.98 E-5 |
| Cs | 3.27 E-7 | 3.60 E-7 |

The simulation was executed with 1E6 neutron histories at each of 24 angles around the sample for a total neutron fluence of 1.056E9. Gamma spectra were generated for each projection in the sequence. Gamma counts corresponding to the gamma line from the elements of interest were extracted from each projection to form a sinogram (i.e., variation in gamma counts for that element at each projection in the sequence). A background scatter noise spectrum was then generated using a breast phantom containing only water. An identical number of neutron histories were generated for the background scan, and gamma counts were extracted at each of the energies of interest as above. The background counts were subtracted from the breast signal to correct the neutron and gamma scatter-induced effects observed during the scan. The

resulting background-corrected sinograms were them reconstructed using the maximum likelihood expectation maximization (MLEM) algorithm for emission computed tomography proposed by Lange and Carson [14]. Thirty-two iterations of the algorithm were reconstructed for each element of interest. Four regions-of-interest (ROI) were selected on the image corresponding to the two lesions and to two, equal-sized regions in the breast (outside the lesions). The pixel intensities in the four ROIs were extracted for each image in the series and compared with each other to determine the measured difference between the normal and malignant regions of each breast.

## III. Results

Fig. 3 shows a sample spectrum from a projection acquired using the breast phantom. Some of the prominent gamma lines visible in the spectrum are from $^{12}C$ at 4439 keV and 3927 keV (first escape), $^{1}H$ at 2224 keV (neutron capture), photon annihilation (511 keV) and inelastic scatter gamma lines from Ge in the detectors (595 keV, 834 keV).

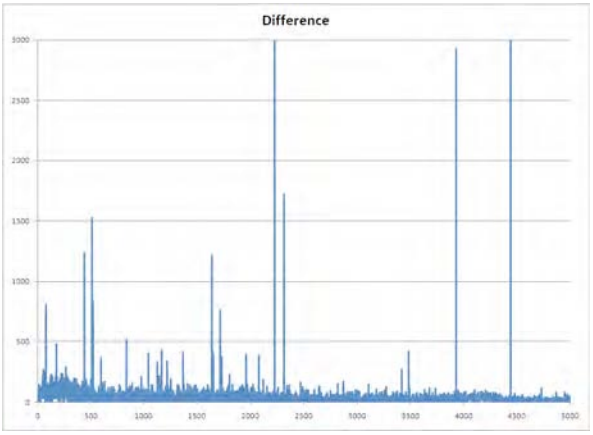


Fig.3. Gamma spectrum from background corrected breast-phantom scan. Prominent gamma lines visible in the spectrum are $^{12}C$ at 4439 keV and 3927 keV (first escape), $^{1}H$ at 2224 keV (neutron capture), photon annihilation (511 keV), and several lines from Ge in the detectors (including 595 keV, 834 keV).

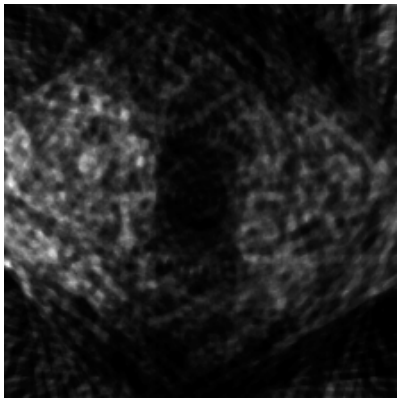

Fig.4. Reconstructed image for $^{12}C$ at 4439 keV corresponding to the FOV shown in Fig.2. The image shows the 3rd iteration of the MLEM algorithm. The location of carbon in the image matches perfectly with the region corresponding to the breast tissue. The right breast shows reduced intensity due to neutron attenuation (the beam entered the image from the left side).

Fig. 4 shows the background-corrected reconstructed image for $^{12}C$ (iteration 3 of the MLEM algorithm) corresponding to the to FOV shown in Fig. 2. The distribution of pixel intensity in the image was found to match perfectly with the regions corresponding to the breasts. This behavior was expected because the original phantom contained carbon-rich tissue only in the breasts. The image verifies the validity of the acquisition and reconstruction technique.

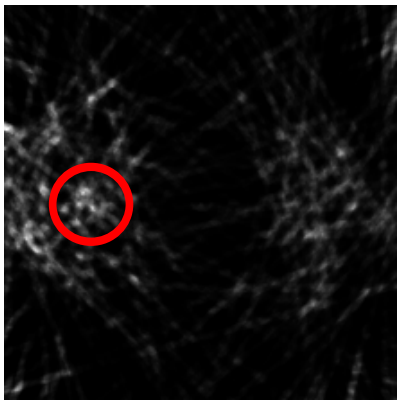

Fig.5. Reconstructed image for $^{23}Na$ (3rd iteration of the MLEM algorithm). The red circle denotes the location of the tumor in the left breast, which shows higher pixel intensity corresponding to an elevated elemental concentration in the malignant tissue.

TABLE II
MEASURED AND EXPECTED INTENSITY RATIOS CORRESPONDING TO THE BEST-PERFORMING ELEMENTS IN THE LEFT BREAST (MAL:NORM).

| Element | Measured Ratio | Expected Ratio | Error |
|---|---|---|---|
| Cs | 0.86 | 1.10 | 22.08% |
| Na | 1.26 | 1.08 | 16.78% |
| Br | 1.06 | 0.93 | 14.31% |
| Zn | 1.09 | 0.98 | 11.87% |

TABLE III
MEASURED AND EXPECTED INTENSITY RATIOS CORRESPONDING TO THE BEST-PERFORMING ELEMENTS IN THE RIGHT BREAST (NORM:MAL).

| Element | Measured Ratio | Expected Ratio | Error |
|---|---|---|---|
| Cs | 1.04 | 0.91 | 14.29% |
| Br | 1.26 | 1.08 | 16.78% |
| Zn | 1.07 | 1.02 | 4.90% |

Similar images were reconstructed for all of the trace elements shown in Table 1. Four of the images, corresponding to bromine, cesium, sodium and zinc, showed statistically significant differences between the two lesions and their backgrounds with measurement errors below 25%. Fig. 5 shows the background-corrected reconstructed image for $^{23}Na$ (iteration 3 of MLEM) corresponding to the FOV shown in Fig.2. In the original phantom, the left breast contained normal tissue with a malignant lesion. The expected ratio of $^{23}Na$ in

the malignant breast to the normal tissue lesion was 1.26 (from Table 1). The measured intensity in the lesion ROI was 57.05 vs. 45.32 in the breast ROI, corresponding to a ratio of 1.08. This represents an error of less than 17%. The measured and expected ratios of the malignant and normal tissue intensities for each breast are shown in Tables 2 and 3.

## IV. Conclusion and Future work

The results indicate the capability of the NSECT imaging system in generating tomographic images of breast tumors to differentiate between normal and malignant tissue based on trace elemental signatures. In previous studies, we determined that Br and Rb were strong candidates for quantitative differentiation between normal and malignant tissue [3]. In addition to these elements, Cs, Na and Zn may be other promising candidate for tumor identification through imaging. The dose from this scan was approximately 10 mSv, which corresponds to a high-dose, high-accuracy acquisition of the entire breast volume that includes both breasts. In a clinical environment, it may be more feasible to use NSECT in conjunction with a low-dose imaging alternative to allow focusing of the dose in regions of suspicion. We are currently investigating the performance of each of these elements as well as multi-element ratios in differentiating normal and malignant tissue lesions in such low-dose scenarios.

## References


[1] A. J. Kapadia, A. C. Sharma, J. E. Bender, G. D. Tourassi, C. R. Howell, A. S. Crowell, M. R. Kiser, B. P. Harrawood, and C. E. Floyd, "Neutron Stimulated Emission Computed Tomography for Diagnosis of Breast Cancer," *IEEE Trans Nuc Sci*, vol. 55, pp. 501 - 509, 2008.

[2] C. E. Floyd, J. E. Bender, B. P. Harrawood, A. C. Sharma, A. J. Kapadia, G. D. Tourassi, J. Y. Lo, and C. R. Howell, "Breast cancer diagnosis using Neutron Stimulated Emission Computed Tomography: Dose and Count requirements," in *SPIE Symposium on Medical Imaging*, San Diego, CA, 2006, pp. 597-603.

[3] J. E. Bender, A. J. Kapadia, A. C. Sharma, G. D. Tourassi, B. P. Harrawood, and C. E. Floyd, "Breast cancer detection using Neutron Stimulated Emission Computed Tomography: prominent elements and dose requirements," *Med Phys*, vol. 34, pp. 3866-3871, 2007.

[4] A. J. Kapadia, "Neutron Stimulated Emission Computed Tomography: A New Technique for Spectroscopic Medical Imaging," in *Neutron Imaging and Applications*, I. S. Anderson, R. McGreevy, and H. Z. Bilheux, Eds.: Springer, 2009.

[5] H. Mussalo-Rauhamaa, S. Piepponen, J. Lehto, R. Kauppila, and O. Auvinen, "Cu, Zn, Se and Mg concentrations in breast fat of Finnish breast cancer patients and healthy controls," *Trace Elements in Medicine*, vol. 10, pp. 13-15, 1993.

[6] K. Geraki, M. J. Farquharson, and D. A. Bradley, "Concentrations of Fe, Cu and Zn in breast tissue: a synchrotron XRF study," *Phys Med Biol*, vol. 47, pp. 2327-39, Jul 7 2002.

[7] H. D. Wu, S. Y. Chou, D. R. Chen, and H. W. Kuo, "Differentiation of serum levels of trace elements in normal and malignant breast patients," *Biol Trace Elem Res*, vol. 113, pp. 9-18, Oct 2006.

[8] H. W. Kuo, S. F. Chen, C. C. Wu, D. R. Chen, and J. H. Lee, "Serum and tissue trace elements in patients with breast cancer in Taiwan," *Biol Trace Elem Res*, vol. 89, pp. 1-11, Oct 2002.

[9] T. Magalova, V. Bella, A. Brtkova, I. Beno, M. Kudlackova, and K. Volkovova, "Copper, zinc and superoxide dismutase in precancerous, benign diseases and gastric, colorectal and breast cancer," *Neoplasma*, vol. 46, pp. 100-4, 1999.

[10] S. K. Gupta, V. K. Shukla, M. P. Vaidya, S. K. Roy, and S. Gupta, "Serum trace elements and Cu/Zn ratio in breast cancer patients," *J Surg Oncol*, vol. 46, pp. 178-81, Mar 1991.

[11] F. Cavallo, M. Gerber, E. Marubini, S. Richardson, A. Barbieri, A. Costa, A. DeCarli, and H. Pujol, "Zinc and copper in breast cancer. A joint study in northern Italy and southern France," *Cancer*, vol. 67, pp. 738-45, Feb 1 1991.

[12] V. N. Ivanchenko, "Geant4 toolkit for simulation of HEP experiments," *Nuclear Instruments and Methods in Physics Research Section A*, vol. 502, pp. 666-668 2003.

[13] S. Agostinelli, J. Allison, K. Amako, J. Apostolakis, H. Araujo, P. Arce, M. Asai, D. Axen, S. Banerjee, G. Barrand, F. Behner, L. Bellagamba, J. Boudreau, L. Broglia, A. Brunengo, H. Burkhardt, S. Chauvie, J. Chuma, R. Chytracek, and G. Cooperman, "GEANT4: A Simulation Toolkit," *Nuclear Instruments and Methods in Physics Research NIM A*, vol. 506, pp. 250-303, 2003.

[14] K. Lange and R. Carson, "EM reconstruction Algorithms for Emission and Transmission Tomography," *Journal of Computer Assisted Tomography*, vol. 8, pp. 306-316, 1984.

# Sensitivity analysis for liver iron measurement through neutron stimulated emission computed tomography

**G A Agasthya[1,2,3] , B C Harrawood[1,2,4], J P Shah[1,2,3] and A J Kapadia[1,2,4]**
1. Duke University, Durham, North Carolina, USA.
1. Carl E. Ravin Advanced Imaging Labs, Duke University, Durham, North Carolina, USA.
1. Biomedical Engineering Department, Duke University, Durham, North Carolina, USA.
1. Radiology Department, Duke University, Durham, North Carolina, USA.
E-mail: greeshma.agasthya@duke.edu
anuj.kapadia@duke.edu

**Abstract.** Neutron Stimulated Emission Computed Tomography (NSECT) is being developed as a non-invasive imaging modality to detect, quantify and localize iron overload in the human liver. NSECT uses gamma photons emitted by the inelastic interaction between monochromatic fast neutrons and iron nuclei to detect and quantify iron overload. Previous GEANT4 simulation studies as well as experiments with phantoms have shown that NSECT has the potential to diagnose iron overload with reasonable levels of radiation dose. This simulation study was conducted to determine the sensitivity of the NSECT system for different patient sizes. A GEANT4 simulation of the NSECT system was developed with multiple human liver and torso sizes to determine the sensitivity of the system. The liver was simulated with liver iron concentrations between 0.5-20 mg/g (wet). HPGe gamma detectors were simulated to detect the emitted gamma spectrum. The gamma spectra of multiple iron concentrations and patient sizes were background corrected with spectra from water phantoms. The obtained corrected gamma spectra were analyzed to determine the sensitivity of the NSECT system. These analyses indicate that the sensitivity of the NSECT system for different adult patient sizes (Torso volumes between approximately 15000 $cm^3$ to 29000 $cm^3$) lies between 0.5 mg/g to 2 mg/g (wet). These iron concentrations represent a range that is clinically significant for human iron overload.

## 1. Introduction:

The liver is a vital organ and plays a major role in metabolism. It detoxifies blood, synthesizes proteins and produces digestive juices (Widmaier, Raff et al. 2008). Liver iron overload or hemochromatosis is a disorder of the liver that is characterized by an increase in the liver's iron content. It may be caused due to genetic or acquired factors, and if untreated, it may lead to tissue damage, liver cirrhosis, hepatic failure, cardiac failure, hepatocellular carcinoma and diabetes (Powell 2005). Detection and monitoring of iron levels in the liver are of prime importance for the evaluation of a treatment response. Presently, percutaneous liver biopsy is the most reliable method of quantifying liver iron overload (Bernardino 1984). However, hepatic biopsy apart from being invasive, can lead to retroperitoneal bleeding, subcapsular hematomas, septic shock and formation of fistula between various biliary channels (Bernardino 1984). Advanced Magnetic resonance imaging (MRI) techniques are being developed and used to non-invasively image liver iron overload. Conventional T2- and T2* weighted MRI is used for the qualitative detection of liver iron overload. Some other techniques like in-phase and out-of-phase imaging described by Dixon in 1984 and a gradient-echo based technique described by Gandon et al have tried to indirectly quantify liver iron concentrations (Gandon, Guyader et al. 1994; Taouli, Ehman et al.

2009). Some of the disadvantages of these MRI techniques are lack of quantitative information, absence of a direct method of iron measurement and the confounding results obtained due to the presence of fat and other abnormal tissue. To avoid the risks associated with biopsy and overcome the disadvantages of MRI, we are developing a technique called neutron stimulated emission computed tomography (NSECT) as a non-invasive alternative for liver iron measurement to monitor the progress of hemochromatosis in patients (Kapadia, Floyd et al. 2005 ).

NSECT is a non-invasive, spectroscopic technique capable of quantifying the concentration of an element in biological tissue (Floyd, Bender et al. 2006 ). The principle of the technique is explained as follows: When a fast neutron undergoes inelastic scatter with an atomic nucleus in the body, it excites the nucleus to a higher energy level. The excited nucleus emits characteristic gamma radiation that is unique to the emitting element and can be used as its identifying signature. Analysis of the gamma spectrum emitted from the tissue provides quantitative information about its elemental composition.

The probability of inelastic scattering of neutrons with the nuclei of interest depends on two factors: (a) the inelastic scatter cross-section of the nucleus, and (b) its concentration in the organ. High Purity Germanium (HPGe) gamma detectors are used to generate energy spectra from the emitted gammas. The heights of the gamma lines in the spectrum corresponding to the elemental nuclei of interest are used to quantify the concentration of the element in the organ (Floyd, Bender et al. 2006 ). A simple model of an NSECT system is shown in figure 1. In previous studies, we have demonstrated that NSECT can be used for detection and quantification of liver iron overload with clinically acceptable levels of dose (Kapadia, Tourassi et al. 2008). In the case of iron measurement, when neutrons interact inelastically with $^{56}$Fe nuclei, gamma photons with energies 846.776 keV, 1810.772 keV etc; are emitted (National Nuclear Data Center 2007). These gamma energies represent different excitation states of $^{56}$Fe nuclei and depend on the energy of incident neutrons. The gamma energy line at 846.771 keV (i.e., approximately 847 keV) is the strongest peak, corresponding to $^{56}$Fe, that can be detected with sufficient accuracy above the background noise. To estimate the gamma counts in this peak, we add the counts at 846 keV and 847 keV. This spread in the gamma counts across two adjacent energy channels can be attributed to the energy binning used to generate the gamma spectra. Henceforth, an iron peak refers to the sum of the gamma counts observed at 846 keV and 847 keV.

To implement NSECT as a clinical technique for iron overload detection, it is important to determine its sensitivity in iron quantification. The sensitivity of the NSECT system for the detection of liver iron overload is defined as the minimum concentration of iron that can be detected and quantified accurately. The clinically significant concentration range of liver iron is between 0.5 mg and 20 mg of iron per gram of liver tissue (Wood 2007).

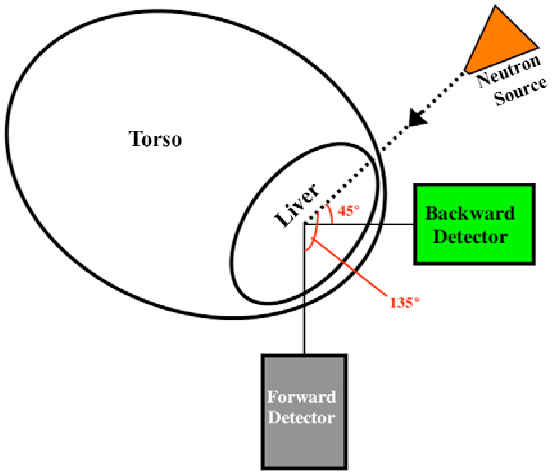


**Figure 1. A simple schematic of an NSECT system. The 'Neutron Source' is the source of a fast neutron beam. The neutron beam can be tuned to the required energy and collimated to any required spatial profile. The detectors are cylindrical HPGe crystals. They can be positioned at any desired location around the sample to achieve maximum efficiency of gamma detection. Here we see one forward and one backward detector. In this figure, the sample shows the axial view of the torso with the inner oval representing the liver.**

The sensitivity of the NSECT system depends on several different factors that can be classified as follows:

a) **Neutron attenuation**: This process follows the Beer-Lambert's attenuation formula (Attix 1986). Neutron attenuation by the tissue sample reduces the number of neutrons available for stimulation of the tissue sample, which consequently reduces the number of gamma photons emitted.

b) **Probability of inelastic scatter**: This depends on the inelastic-scatter cross-section of the nuclei in the tissue, which is dependent on the neutron energy and on the concentration of the nuclei (Attix 1986).

c) **Gamma emission profile**: Each energy transition within a nucleus shows a specific, known emission pattern (e.g. dipole, quadrupole, etc.). Therefore, the overall detection efficiency of the emitted gamma rays depends on the angle at which the detectors are placed. The detectors must be positioned at angles with the maximum probability of gamma emission. For $^{56}$Fe with its quadrupole emission profile, the maximum emission probability occurs at ±45° and ±135° (Jackson 1975).

d) **Gamma attenuation**: Gamma attenuation, similar to the neutron attenuation, follows the Beer-Lambert's attenuation formula. The number of gamma photons incident on the detectors depends on the gamma attenuation by the tissue between the point of emission and the detectors (Attix 1986).

e) **Losses due to detector properties**: Two detector properties influence the observed gamma signal: (i) the distance of the detectors from the point of gamma emission and (ii) the efficiency of the detector crystal. The effect of detector distance follows the inverse square law (Knoll 2000). Ideally the detectors should be placed as close to the tissue as possible. The efficiency of the detector is a property of the individual crystal that is also dependent on the energy of the incident gamma photons. The efficiency of the detector crystal is generally specified by the manufacturer.

In previous work, we have described simulation studies to demonstrate the application of NSECT for the detection of iron overload in patients (Sharma, Harrawood et al. 2007). In this manuscript,

we describe a series of simulation experiments to determine the sensitivity of the NSECT system for the non-invasive quantification of iron in the liver. In this study, we have modeled a uniform diffusion of iron in the liver. In general, liver iron deposits may occur in one of two ways, either diffused uniformly throughout the liver or concentrated in 'lesions' with high iron content (or a mix of the two). In this study, we have considered only the first scenario, i.e., uniformly distributed iron, as a starting point. Three different simulation models of the liver and torso have been developed to evaluate the sensitivity of NSECT at different iron concentrations in differently sized patients.

**2. Methods:**

In this section, we will describe the different simulations developed to study the sensitivity of the NSECT system. All the simulations have been performed in GEANT4, which is a C++ based, high-energy physics, Monte Carlo simulation toolkit (Agostinelli and Collaboration 2003; Ivanchenko 2003). GEANT4 was developed at CERN in Switzerland to simulate the interactions between high-energy particles and matter. It allows the modeling of particle sources, detectors, human anatomy and the accurate estimation of signal obtained from the particle interactions.

In previous studies, we have demonstrated and described the development and modeling of the NSECT system in the GEANT4 environment (Kapadia 2007; Kapadia, Sharma et al. 2007; Sharma, Harrawood et al. 2007; Kapadia 2008; Kapadia, Harrawood et al. 2008; Kapadia, Harrawood et al. 2008). The simulations described in this manuscript are an extension of these previous studies. To determine the sensitivity of NSECT for detection and quantification of hemochromatosis, we developed three different models of the torso and the human liver. The three models differed in the size and the shape of the liver and the torso, neutron and gamma attenuation properties, and number and size of detectors. A summary of the models is shown in table 1. Each model was irradiated using the simulated NSECT system for a predetermined number of neutron histories. Gamma energy spectra were generated for each model in the simulations and were analyzed to obtain the sensitivity of the NSECT system for the detection of liver iron overload. (Note: Although NSECT is a tomographic technique with the ability to generate images of the iron content, this study focuses on simple spectroscopic quantification without any imaging. Imaging applications will be discussed in future experiments).

| Model # | Torso Volume (cmxcmxcm) | Liver | | Detector | | Neutron Beam Energy (MeV) |
|---|---|---|---|---|---|---|
| | | Shape | Volume (cmxcmxcm) | Number | Dimensions* (cmxcm) | |
| 1. | 30x25x11 | Elliptical Tube | 20x10x9 | 2 | 9x8 | 4.5 |
| 2a. | 30x22.5x30 | Approximation of anatomical shape | ≈1400 | 6 | 10x10 | 5.0 |
| 2b. | 40x30x30 | Approximation of anatomical shape | ≈1400 | 6 | 10x10 | 5.0 |

**Table 1. A summary of the simulation models developed in GEANT4. Model 1 was used to study the performance of the NSECT system with varying iron concentrations. Model 2a and 2b provided a comparison of the performance of the NSECT system for different patient sizes. (*Dimensions of detector is defined by diameterxheight of a cylinder)**

*2.1. Simulation Development*

As described in the previous section, the NSECT system contains a neutron gun, HPGe gamma

detectors and the iron-overloaded liver phantom. The neutron gun emits a mono-energetic beam of neutrons with NSECT-relevant energies (usually between 2.5-7.5 MeV). In this experiment, we used two energy values - 4.5 MeV and 5 MeV. This energy is sufficient to stimulate characteristic emission from iron (at 847 keV), nitrogen (at 1635 keV and 2312 keV) and carbon (4.4 MeV) in the tissue sample. The beam profile was square with an area of 0.64 $cm^2$. This narrow beam profile represents a physically realistic scenario and can be used to facilitate tomographic acquisition if required (Floyd, Kapadia et al. 2008). Multiple gamma detectors were used in each of the simulations as shown in table 1. Each gamma detector is a cylinder of natural germanium. The dimensions of the detectors are shown in table 1. The density of germanium in the detector was set at 5.32 $g/cm^3$, i.e., the density of natural germanium at room temperature. The composition of germanium in the detector was set to a mixture of the five most abundant stable isotopes of germanium observed in naturally occurring germanium (Table 2)(National Nuclear Data Center 2007).

| Germanium Isotope | Composition in % |
|---|---|
| Ge 70 | 20.37 |
| Ge 72 | 27.31 |
| Ge 73 | 7.76 |
| Ge 74 | 36.73 |
| Ge 76 | 7.83 |

**Table 2. Composition of naturally occurring germanium.**

In the three models (i.e., 1, 2a and 2b), the increase in torso sizes led to an increase in the neutron and gamma attenuation through the tissue. The effect of this increase on the signal provided an estimate of the performance of the NSECT system for different patient sizes. Similarly, the number and position of the detectors directly affects the accuracy of detection of liver iron overload. An increase in the number of detectors leads to an increase in the probability of detection of 847 keV gamma photons (i.e., the $^{56}Fe$ signature energy), and hence increases the accuracy of iron quantification. However, an increase in the number of detectors also significantly increases the cost of the system. Therefore, to maximize the detection probability using the minimal number of detectors, they must be positioned at an optimal angle based on the known gamma emission profile of $^{56}Fe$. Optimal placement increases the probability of detection of 847 keV gamma photons, thereby increasing the accuracy of detection. Each of these factors has been included in the simulation.

The three models developed for this study are explained below.

**Model 1:** Model 1 was developed to investigate the relationship between the signal (at 847 keV) and the concentration of iron in the liver. The model includes two HPGe detectors, which represents the configuration used in a previous experiment (Kapadia, Tourassi et al. 2008). The neutron beam is mono-energetic (4.5 MeV) and exhibits a square profile (0.64 $cm^2$). The liver model is based on a generalized simulation of an adult human torso. Figure 2a shows the top view of model 1.

Torso: In this model the torso is an elliptical tube (yellow oval in figure 2a) with the following properties:

Torso major axis: 30 cm
Torso minor axis: 25 cm

Torso height: 11 cm
Torso material: Water
Torso material density: 1 g/cm$^3$

These sizes are based on the average sizes of an adult human torso. The material of the torso is set to water because water exhibits similar neutron and gamma attenuation coefficients and scattering properties as the human body (Kapadia 2008), and can mimic the signal losses and noise effects generated by the human body.

Liver: In model 1, the liver phantom is an elliptical tube (solid pink oval in figure 2a) with a volume of approximately 1400 cm$^3$. The liver volume was approximated to the average volume of an adult human liver. The shape of the liver, modeled as an elliptical tube, was adequate to investigate the relationship between the gamma signal and the iron concentration (mg/g wet) in the liver for sensitivity analysis. The liver was placed at the right side of the torso, similar to the anatomic location of the human liver in the body, which is present in the right upper quadrant of the abdominal cavity.

In this model the liver exhibits the following properties:

Liver major axis: 20 cm
Liver minor axis: 10 cm
Liver height: 9 cm
Liver material: Elemental composition of healthy adult liver as mentioned in ICRU report 46 (ICRU 1992).
Liver material density: 1.071 g/cm$^3$
Liver volume: 1410 cm$^3$

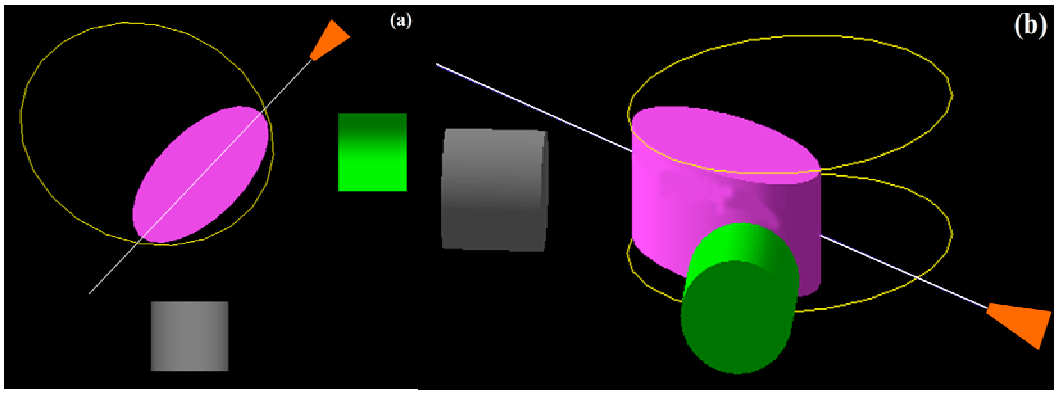


**Figure 2a. Top view of model 1. The yellow oval represents the torso boundary. The pink solid oval within the torso represents the liver. The green and grey rectangles are the top views of the germanium detectors. 2b. Orthogonal view of model 1. The orange triangle represents the neutron source and white line represents the neutron beam path. The green detector is positioned at +45º with respect to the beam and the grey detector is positioned at +135º with respect to the beam.**

Neutron source: The neutron source is positioned in a manner that ensures beam incidence along the major axis of the liver. The neutron beam path through the torso and liver is shown in figure 2b.

Detectors: In this model, we used two germanium detectors to acquire the gamma signal. The properties of the detectors are as follows:

Detector height: 8 cm
Detector diameter: 9 cm
Detector material: Mix of 5 stable germanium isotopes shown in table 2
Detector material density: 5.32 g/cm$^3$

The positions of the detectors, measured with respect to the neutron beam path at the center of the liver (shown in figure 1), were +135º (grey detector in figure 1, the forward angle detector), and +45º (green detector in figure 1, the backward angle detector). Although the forward angle detector receives maximum signal from the liver, it also receives a high fraction of forward-scattered neutrons, electrons and low-energy gamma photons, which reduce the overall signal to noise ratio (SNR). Similarly, although the backward angle detector receives fewer gamma photons at the energy of interest, it exhibits high SNR due to the reduced incidence of scattered neutrons, electrons and low energy gamma photons at the backward angle. The reduced incidence of scattered neutrons also reduces the neutron-induced damage to the detector. Therefore, backward-angle geometries are critical for NSECT acquisition. In this model, we have used one backward angle detector and one forward angle detector to investigate the effect of the detector direction (i.e., forward vs. backward) on the signal and sensitivity of the NSECT system. The 45º and 135º angles were chosen to match the locations of maxima in the quadrupole gamma emission profile of $^{56}$Fe. The -45º and -135º positions were rejected because their proximity to the torso would lead to maximum detection of neutron and gamma scatter noise originating from the torso instead of the desired signal from the liver tissue. The detectors were placed at a distance of 15 cm from the center of the liver to accommodate the translation of the scanner (which, although not used here, is required in the case of tomography).

The iron in model 1 was distributed uniformly throughout the liver with concentrations between 0.5 and 20 mg of iron per gram of liver tissue (i.e., mg/g, wet), which represent the extreme limits reported in literature (Wood 2007). Theoretically, we expect a linear relationship in the emitted gamma signal with the iron concentration in the liver. The minimum concentration of iron that conforms to the expected linear trend is defined as the sensitivity limit of the system.

**Model 2:** This model investigates the effect of patient size on the detected signal. In this model, two patient torso sizes were modeled as shown in table 3. The size of the torso was the only difference between model 2a and model 2b; the size of the liver in both cases was identical. An increase in the patient size leads to an increase in the neutron and gamma attenuation in the torso, which decreases the signal from the desired element, i.e., $^{56}$Fe, and increases the incidence of scattered neutrons and gamma photons on the detectors. The increased incidence of neutrons and gamma photons on the detectors leads to higher detector noise through inelastic scattering interactions and Compton scattering, which leads to a decrease in the overall sensitivity. In model 2 the spine was modeled in the torso with bone material.

| Model | Torso | | Spine diameter in cm | Detector distance in cm |
|---|---|---|---|---|
| | Major axis in cm | Minor axis in cm | | |
| 2a | 30.0 | 22.5 | 3.0 | 15.0 |
| 2b | 40.0 | 30.0 | 4.0 | 17.25 |

**Table 3. A summary of the two patient torso sizes in model 2. The detector distance is the distance from the center of the liver to the detector face.**

**Model 2a:** This model was given the smaller torso size of the two, as shown in table 3. The model contains six HPGe detectors. The neutron beam is mono-energetic (5.0 MeV), with a square profile (0.64 $cm^2$). Figure 3a shows the top view of model 2a.

Torso: In model 2a, the torso is an elliptical tube (yellow oval in figure 3a) with the following properties:

Torso major axis: 30 cm
Torso minor axis: 22.5 cm
Torso height: 30 cm
Torso material: Water
Torso material density: 1 $g/cm^3$

The perimeter of the torso was set to the size of an average adult human torso. A 30-cm transverse section (i.e., height) was simulated to obtain an accurate estimate of the noise generated in the torso. This transverse section of the torso contained the spine and the liver. The material of the torso was set to water, which exhibits similar neutron and gamma attenuation coefficients as the human body (Kapadia, Sharma et al. 2006) and mimics the signal losses and noise effects generated by the human body.

Spine: The spine was positioned close to one edge of the minor axis (solid white circle shown in figure 3a).
The spine was simulated with the following properties:

Spine radius: 1.5 cm
Spine height: 30 cm = Torso height
Spine material: Elemental composition of bone as mentioned in ICRU report 46 (ICRU 1992).

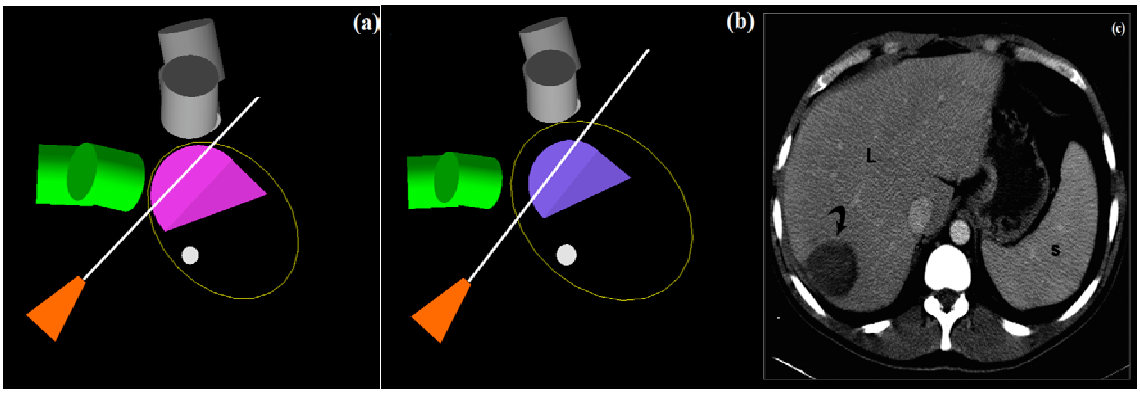


**Figure 3a. Top view of model 2a (torso major axis = 30 cm). The yellow oval represents the torso boundary. The solid pink structure within the torso represents the liver. The solid white circle represents the spine. The green and grey cylinders are the germanium detectors. 3b. Top view of model 2b (torso major axis = 40 cm). The yellow oval represents the torso boundary. The solid violet structure within the torso represents the liver. The solid white circle represents the spine. The green and grey cylinders are the germanium detectors placed at 45º and 135º with respect to the neutron beam. In both 3a and 3b, the white line represents the neutron beam path and the orange polygon is the neutron source. 3c) Top view of a liver (L) as seen in a CT scan (Tsirigotis P). Similar CT scan images of the liver were used to determine the shape and volume of the liver in models 2a and 2b.**

Liver: The liver in models 2a and 2b (identical size and shape in both models) was modeled as a Boolean combination of multiple solid structures to approximate the anatomical shape and size of an average adult human liver with a volume of approximately 1400 $cm^3$. The shape and volume were determined from CT scan images of the human liver; an example of a liver CT scan is shown in figure 3c (Tsirigotis P). The detailed structure of the simulated liver can be seen in figure 4. The iron in the liver was distributed uniformly as described in model 1.

Detectors: In model 2a, we used six germanium detectors; the properties of the detectors are described in the description of model 2b below.

**Model 2b:** This model was given the larger torso size of the two, as shown in table 3. The model contains six HPGe detectors. The neutron beam is mono-energetic (5.0 MeV), with a square profile (0.64 $cm^2$). Figure 3b shows the top view of model 2b.

Torso: In model 2b, the torso was an elliptical tube (yellow oval in figure 3b) with the following properties:

Torso major axis: 40 cm
Torso minor axis: 30 cm
Torso height: 30 cm
Torso material: Water
Torso material density: 1 $g/cm^3$

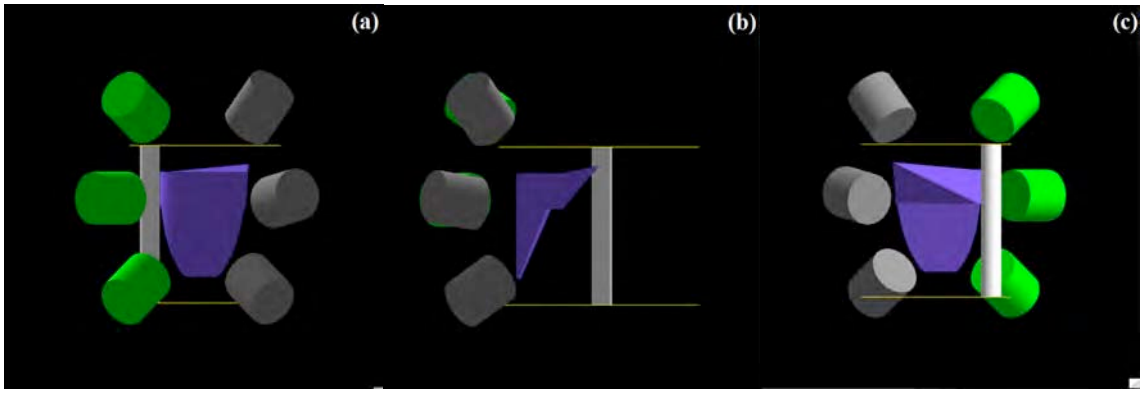


**Figure 4a. Detectors positioned to face the center of the Liver at a distance ≥ 15cm from the center of the liver. 4b. Coronal View of the liver, seen also is the spinal cord. 4c. The top two and bottom two detectors are tilted by angles± 45º.**

Liver: The properties of the liver, including the shape and size, are identical to those of model 2a above. Despite the larger torso size, the volume of the liver was maintained at 1400 $cm^3$ to maintain constant signal from iron and hence, restrict the effects on the signal to the patient size only.

Detectors: In models 2a and 2b, six detectors were placed symmetrically around the center of the liver at a distance of 15 cm and 17.25 cm from the center of the liver, respectively. The larger distance in model 2b was required to accommodate the larger patient size. The three green cylinders shown in figure 4 are the three backward-angle detectors positioned at 45º. The top and bottom backward-angle detectors were rotated by azimuthal angles of +45º and -45º, respectively, to ensure that the front faces of the detectors faced the center of the liver. Similarly, the three forward-angle detectors (represented by grey cylinders in figure 4) were placed in the 135º plane

facing the center of the liver. The symmetric arrangement of the six detectors is shown in figure 4. The angles +45º and +135º were selected for the same reasons as explained in model 1.

*2.2. Data acquisition*

The concentration of iron in models 1, 2a and 2b was varied from 0.5 mg/g (wet) to 20 mg/g (wet). At each concentration, 20 million neutron histories were generated with the neutron source illuminating the torso and the liver. The inelastically stimulated nuclear gamma emission was detected and reported by the HPGe detectors. Other particles such as electrons, positrons and low energy neutrons were also generated through neutron-tissue interactions and were incident on the gamma detectors. The energy deposited in the detectors by these interactions was also reported in the detector output. The detected gamma energies were discretized into 1-keV bins and plotted as a frequency distribution, i.e., an energy spectrum. The spectra for each detector were analyzed separately to obtain a measure of the signal from iron.

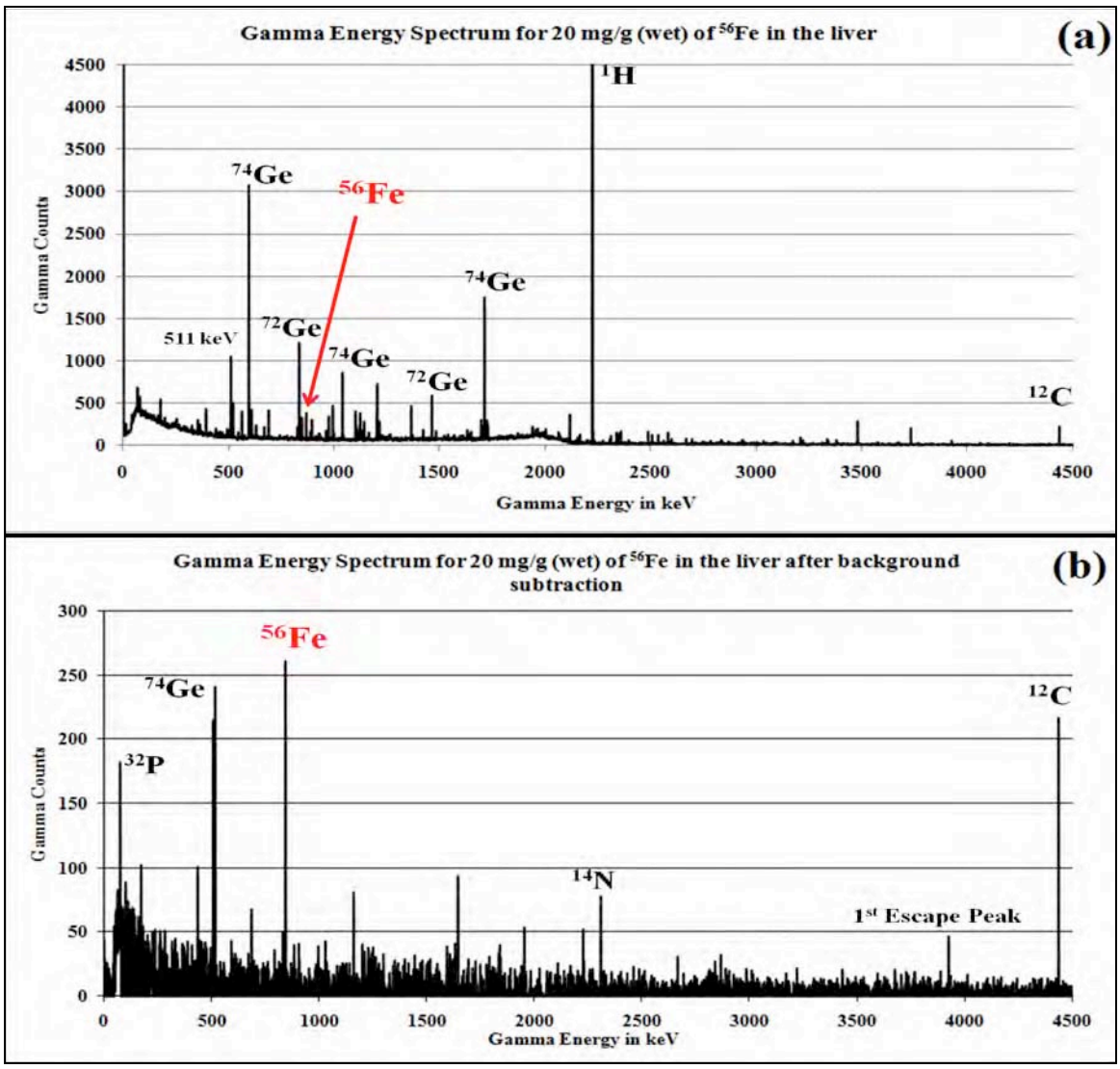


**Figure 5a. Example of a low-SNR signal from the HPGe detector. The major peaks are labeled. After background subtraction, we expect the peaks from germanium and hydrogen**

**and the noise from Compton scattering to be significantly reduced. 5b. Spectrum after background subtraction. The large peaks from hydrogen and germanium are almost eliminated. The prominent peaks from elements present in the tissue (i.e., carbon, nitrogen and iron) can be seen more clearly. The peak marked 1st Escape Peak is the escape peak of Carbon. Oxygen is not visible because the neutron energy (4.5 MeV) was not high enough to stimulate the oxygen nucleus.**

Figure 5a shows a sample spectrum generated using the simulated system. In this spectrum, the iron signal is expected to appear at 847 keV. The signal shows low SNR, primarily due to the large contributions from Compton scattering of high-energy gamma photons in the detectors. To increase the SNR of the signal, we performed background subtraction as follows: The material in the liver was replaced with water to form a 'background' water model. This water model was scanned using 20 million neutron histories in a manner similar to the liver iron scans. The resulting spectrum provided an estimate of the neutron and gamma scatter-related noise in the model, including the noise from materials outside the torso (e.g., germanium). The background spectrum was then subtracted from the low-SNR spectrum. Figure 5b shows the spectrum after background subtraction. Such background-corrected spectra were generated individually for each detector and then added to obtain a single spectrum for each iron concentration per model. From each spectrum we calculated the number of gamma counts in the iron peak.

The statistical significance of detecting the iron peak above the residual background was determined using Student's t-test, with $p \leq 0.05$ considered statistically significant. The average residual background was determined for the region between 800 keV and 900 keV after manually eliminating the peaks from germanium. The calculated average was multiplied by two to compensate for the summing of two energy channels in the iron peak. Peaks detected above background with $p > 0.05$ were excluded from the analysis.

Following this, the percent error was calculated with respect to the expected counts. The expected counts were obtained by fitting a line to the simulated gamma-count data. The results obtained are discussed in the next section.

## 3. RESULTS:

### *3.1. Model 1*

In model 1, a uniform distribution of iron in the liver was scanned with 20 million neutron histories and two HPGe detectors - one at a backward angle and one at a forward angle. The signal from the two detectors was added to obtain the spectrum shown in figure 5a. The background corrected spectrum is shown in figure 5b. Figure 6 shows a close up of the iron peak in the background-corrected spectrum. This peak corresponds to gamma counts from the 20-mg/g concentration of iron.

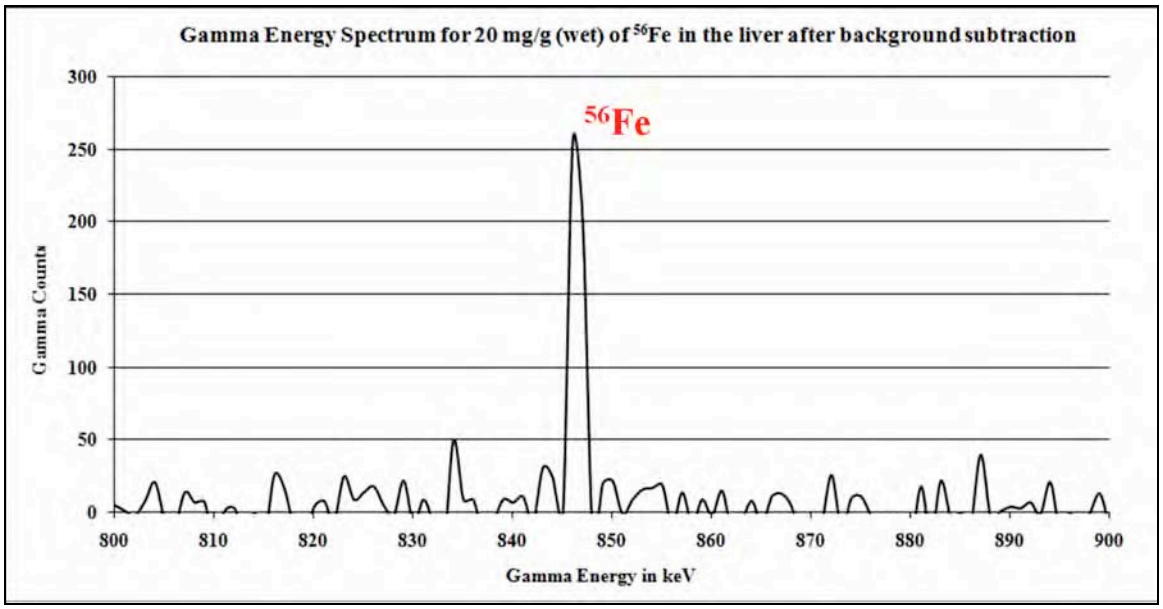


**Figure 6. The gamma peak at 847 keV for the 20-mg/g (wet) concentration of iron in the liver. This spectrum is obtained after background subtraction.**

Similar background corrected spectra were generated for iron concentrations: 0.5 mg/g, 0.75 mg/g, 1 mg/g, 2mg/g, 3mg/g, 4 mg/g, 5 mg/g, 6 mg/g, 7mg/g, 8mg/g, 9mg/g, 10 mg/g, 11 mg/g, 12 mg/g, 13 mg/g, 14 mg/g, 15 mg/g, 16 mg/g, 17 mg/g, 18 mg/g, 19 mg/g and 20 mg/g (wet). Figure 7 shows a plot of the background-corrected gamma counts from iron vs. the iron concentration in the liver. As seen in figure 7, the gamma counts show a highly linear relationship with the iron concentration.

The error bars in figure 7 represent the standard deviations for each measured value of gamma counts. Table 4 shows the gamma counts (Ip), residual background (Rb), p-values and the percent error for each iron concentration investigated in the simulation. The following two conditions were imposed to determine the sensitivity of the NSECT system for liver iron detection: A) The gamma counts must conform to the expected linear relationship with the iron concentration, and B) The gamma signal must be detected above background with $p \leq 0.05$. The expected counts at each concentration were calculated from the fitted linear trend line. The percent error was calculated with respect to the expected counts.

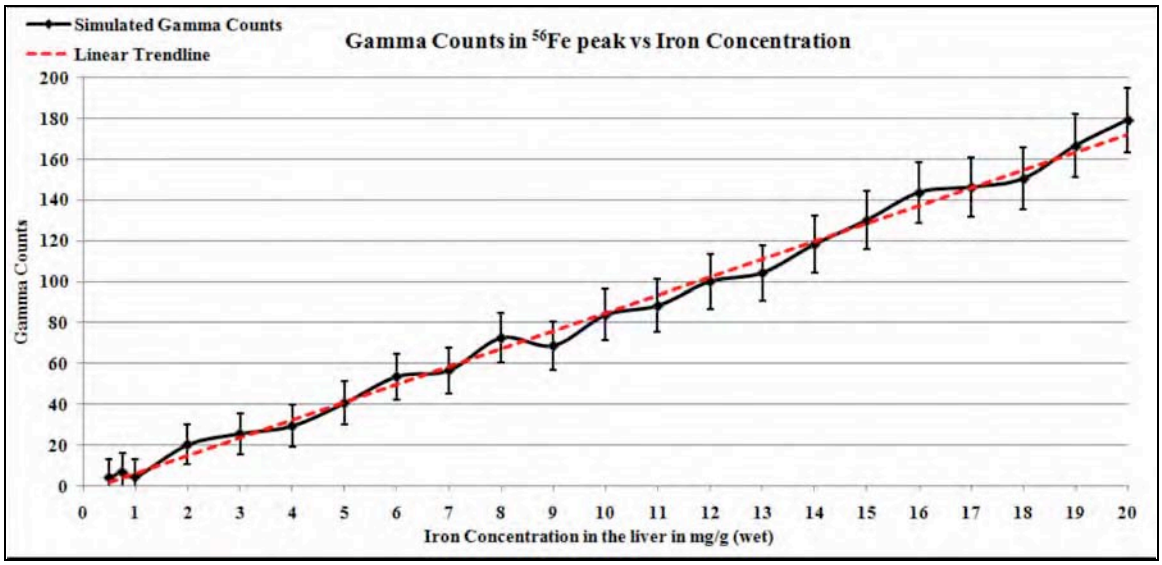


**Figure 7. Plot of the gamma counts vs. iron concentration in the liver. The solid black line represents the measured gamma counts obtained from the simulation. The red dotted line represents the expected counts obtained by fitting a linear trend line to the simulated counts. The error bars represent the standard deviation of the measured values.**

| Iron Concentration in mg/g (wet) | Gamma counts in iron peak (Ip) | Residual background counts (Rb) | p-value ($p < 0.05$) | Percent error |
|---|---|---|---|---|
| 0.5 | 4 | 4.8 | 3.90E-01 | 99.86 |
| 0.75 | 6.8 | 4.8 | 2.59E-01 | 62.48 |
| 1 | 4.4 | 4.8 | 4.37E-01 | 30.91 |
| 2 | 20.2 | 5.0 | 4.07E-04 | 33.74 |
| 3 | 25.6 | 4.9 | 5.21E-05 | 7.39 |
| 4 | 29.4 | 4.9 | 1.71E-05 | 9.74 |
| 5 | 40.6 | 4.7 | 1.14E-06 | 1.72 |
| 6 | 53.6 | 6.9 | 1.90E-07 | 7.11 |
| 7 | 56.6 | 5.1 | 9.07E-08 | 3.71 |
| 8 | 72.6 | 5.1 | 1.42E-08 | 7.53 |
| 9 | 68.8 | 5.2 | 2.13E-08 | 9.77 |
| 10 | 83.8 | 5.4 | 5.24E-09 | 1.39 |
| 11 | 88.4 | 5.8 | 3.76E-09 | 5.67 |
| 12 | 100 | 5.8 | 1.58E-09 | 2.39 |
| 13 | 104.2 | 5.4 | 1.15E-09 | 6.28 |
| 14 | 118.2 | 5.9 | 5.20E-10 | 1.44 |
| 15 | 130 | 6.2 | 2.82E-10 | 1.04 |
| 16 | 143.6 | 5.4 | 1.41E-10 | 4.52 |
| 17 | 146.2 | 5.8 | 1.29E-10 | 0.05 |
| 18 | 150.4 | 5.9 | 1.09E-10 | 2.88 |
| 19 | 166.6 | 6.3 | 5.88E-11 | 1.84 |
| 20 | 179.2 | 7.0 | 3.89E-11 | 3.99 |

**Table 4. The gamma counts in the iron peak (Ip), the average residual background counts (Rb) in the spectra after background correction and p-values corresponding to the liver iron concentrations in model 1.**

From figure 7 and table 4, we see that the linearity in the trend was maintained down to 2 mg/g but not at the lower values. All concentration values above (and including) 2 mg/g satisfied the two conditions imposed for sensitivity determination. As shown in table 4, the gamma counts corresponding to 0.5 mg/g, 0.75 mg/g and 1 mg/g could not be detected above background with sufficient statistical significance. From these observations, we inferred that the NSECT system can detect liver iron concentrations between 1-2 mg/g.

*3.2. Models 2a and 2b*

In this simulation, we compared the sensitivity of the NSECT system for two different patient sizes, Model 2a (Torso major axis = 30 cm, Torso Volume = 15,904.31 $cm^3$) and Model 2b (Torso major axis = 40 cm, Torso Volume = 28,274.33 $cm^3$). From the previous experiment with Model 1, we determined that the NSECT system was sensitive to liver iron concentrations above 2 mg/g. Therefore, in this model, we focused on the lower concentration ranges and sampled only a few high concentration values. Data were generated for the following iron concentrations: 0.5 mg/g, 1 mg/g, 2mg/g, 3mg/g, 4 mg/g, 5 mg/g, 10 mg/g and 20 mg/g (wet).

We expected a decrease in signal due to the increase in the patient size; to compensate for this decrease, the number of detectors around the torso was increased to six. Figure 8 shows the gamma counts obtained with the six detectors positioned around the torso (the detector positions are shown in figure 4a). Figure 8 also shows the expected counts and error bars for the measured signal. The expected counts were calculated from the fitted linear trend line. The error bars represent the standard deviations for each measured value of gamma counts. The summary of the t-test results, gamma counts from the simulation and the calculated percent errors for models 2a and 2b are shown in table 5.

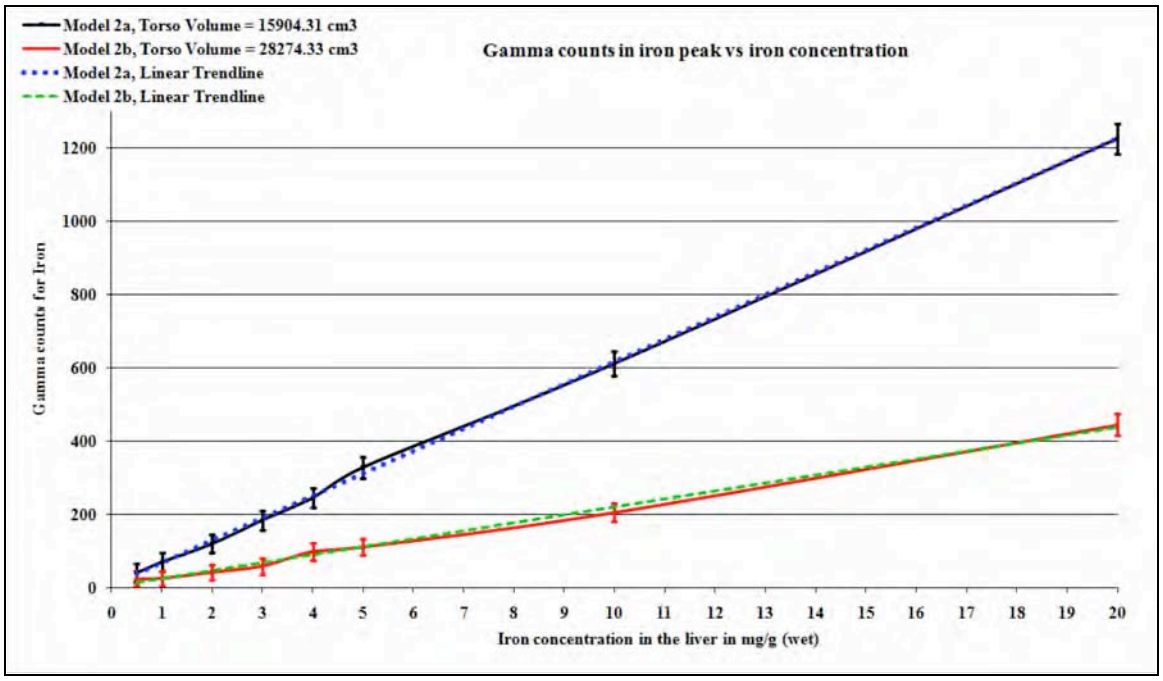


**Figure 8. The measured and expected gamma signal from models 2a (30-cm torso) and 2b (40-cm torso). The gamma counts were normalized to a neutron fluence of 20 million*. The**

**error bars represent the standard deviation. The blue dotted line and the green dashed line represent the expected gamma counts for models 2a and 2b, respectively, obtained by fitting a line to the simulated gamma counts.**

| Iron Concentration in mg/g (wet) | Model 2a | | | Model 2b | | |
|---|---|---|---|---|---|---|
| | Gamma Counts in Iron Peak | p-value | Percent error | Gamma Counts in Iron Peak | p-value | Percent error |
| 0.5 | 40.4 | 6.61E-03 | 8.98 | 23 | 0.1099 | 79.61 |
| 1 | 69.6 | 5.70E-05 | 3.11 | 25.2 | 0.0380 | 6.43 |
| 2 | 119.8 | 3.00E-07 | 6.67 | 41.2 | 1.07E-03 | 9.29 |
| 3 | 184.4 | 5.24E-09 | 2.55 | 58.4 | 7.46E-05 | 13.05 |
| 4 | 245 | 4.50E-10 | 2.04 | 98.2 | 7.04E-07 | 10.45 |
| 5 | 328 | 4.33E-11 | 5.48 | 110.4 | 1.94E-07 | 0.23 |
| 10 | 611 | 5.14E-13 | 0.70 | 204.6 | 5.90E-10 | 6.73 |
| 20 | 1224.2 | 5.86E-15 | 0.02 | 443.8 | 2.49E-12 | 1.60 |

**Table 5. A comparison of gamma counts, p-values and percent errors for the two different patient sizes for eight different concentrations of iron.**

***A neutron fluence of 100 million was simulated to generate data from models 2a and 2b. The gamma counts shown in figure 8 were obtained by normalizing the counts for a neutron fluence of 20 million.**

From the results in figure 8 and table 5, we observed the following:

a) The NSECT system exhibited stronger signal when the neutron and gamma attenuation were lower as in the case of the smaller patient (model 2a), i.e., the NSECT system performed better for the smaller patient.
b) The signal obtained from the smaller patient (Model 2a) was statistically significant for the entire iron concentration range from 0.5 mg/g to 20 mg/g.
c) The signal obtained from the larger patient (Model 2b) was statistically significant for the iron concentration range from 1 mg/g to 20 mg/g.

From these observations, we inferred that the NSECT system with six detectors can detect liver iron concentrations between 0.5-1 mg/g in adults.

**4. Discussion:**

This paper describes a simulation study performed to determine the sensitivity of the NSECT system for non-invasive diagnosis of liver iron overload in patients of different sizes. Medical literature reports patients with iron concentrations between 1.8 mg/g (moderate) and 20 mg/g (severe) as cases of iron overload (Powell, George et al. 1998; Powell 2002; Powell 2005; Wood 2007). The results from our study suggest that the sensitivity of the NSECT system overlaps perfectly with this clinical range of liver iron concentrations. Concentrations between 0.5-20 mg/g were simulated in this study. The results indicated that the sensitivity of the NSECT system lies between 1-2 mg/g of iron in the liver, depending on the number of detectors used and the size of the patient. The 2 mg/g sensitivity limit represents a clinically realistic scenario, which considered a large patient scanned with two HPGe detectors. Our study used GEANT4 to simulate the NSECT system and patient acquisition protocols. The simulated NSECT system was used to generate data from 20 million neutron events for the study.

Three different torso-liver models were simulated to study the sensitivity of the NSECT system. The three models simulated different sizes and volumes of the torso, and used different numbers of gamma detectors. The different combinations were used to study the effect of patient size on the sensitivity of the NSECT system. Increase in the patient size leads to an increase in neutron and gamma attenuation due to the additional tissue. Increase in patient size also contributes to an increase in detector background noise due to the increased scatter of high-energy neutrons and gamma photons in the torso. These factors lead to a decrease in the detected signal (i.e., 847 keV gamma photons emitted from inelastic scatter of neutrons with $^{56}$Fe nuclei). The results from the study indicated that the strength of the signal decreased with increase in patient size (as expected). The detected signal was found to be approximately 3 times lower for every 10-cm increase in patient size (Kapadia, Agasthya et al. 2009). The sensitivity of the NSECT system worsened with an increase in the patient size.

The position and number of HPGe gamma detectors used in acquiring the desired signal also affected the sensitivity of the NSECT system. To achieve increased probability of signal detection and improved SNR, the detector positions were chosen based on the quadrupole gamma emission profile of $^{56}$Fe. To achieve improved accuracy of detection of iron overload the number of detectors were increased. The increased number of detectors, although increased the noise due to scatter from adjacent detectors, resulted in an overall increase in SNR. Model 1 had two gamma detectors compared to six detectors in models 2a and 2b. The increase in the number of detectors caused the improvement in the detection sensitivity for models 2a and 2b. This was verified by calculating the sensitivity of model 2b (Larger torso volume) from the signal of the two detectors placed in the plane of the beam and ignoring the signal from the remaining fours detectors. The NSECT system with two detectors used to scan the 28,274.33 cm$^3$ torso (model 2b) was unable to detect liver iron concentrations below 3 mg/g (wet) with statistical significance. The results also showed a loss in linearity of trend below 5 mg/g (wet) of iron in the liver. Table 6 shows the results from the two detector analysis for the larger patient. Comparing the results for model 2b with two detectors in table 6 with the results for model 2b with six detectors in table 5 it can be inferred that the sensitivity range improves with increase in number of detectors.

| Liver Iron Concentration (mg/g, wet) | Gamma counts in two detectors | p-value |
|---|---|---|
| 0.5 | -0.6 | Test failed |
| 1 | 8.2 | 0.496 |
| 2 | 15.4 | 0.094 |
| 3 | 24.6 | 2.78E-03 |
| 4 | 35 | 1.57E-04 |
| 5 | 33.8 | 1.24E-04 |
| 10 | 76 | 9.06E-08 |
| 20 | 179.8 | 1.56E-10 |

**Table 6. Summary of results from model 2b (Torso volume =28,274.33 cm$^3$) with 2 detectors. The t-test failed for iron concentration of 0.5 mg/g as no gamma counts were detected above the background noise. The gamma counts corresponding to iron concentrations of 1 mg/g and 2mg/g have p-value greater than 0.05 and are not statistically significant. There is a loss in linearity of the trend below 5 mg/g of liver iron concentration.**

*4.1. Radiation dose*

The dose delivered to the patient is a critical aspect of NSECT. It has been shown that the dose delivered to the liver and the surrounding tissues with a fluence of 100 million neutrons is approximately 1 mSv (Kapadia 2007). Dose calculation has been explained in detail in previous studies (Kapadia 2007; Kapadia, Sharma et al. 2007; Sharma, Harrawood et al. 2007; Kapadia, Tourassi et al. 2008). The following steps are a summary of the dose calculation to the tissue in the beam path from 20 million neutrons:
Total number of neutrons = $2x10^{7}$
Energy deposited by each 5 MeV neutron = 4.85 MeV (Kapadia, Tourassi et al. 2008)
Total energy deposited (J) = $1.55x10^{-5}$ J
Mass of tissue irradiated in the beam path = $1.37x10^{-2}$ kg
Absorbed Dose (Gy) = $1.13x10^{-3}$ Gy
Effective Dose Equivalent (Sv) = 0.56 mSv

The radiation dose from the NSECT quantification of liver iron in this study is 0.56 mSv. This is well below the dose of an abdominal and pelvic CT exam, which delivers approximately 15 mSv (RSNA 2007).

In conclusion the results described in this study suggest that the sensitivity of NSECT system is inversely proportional to the patient size. The study also suggests that the sensitivity of the NSECT system can be improved by increasing the number of detectors (albeit at the expense of higher system cost). The overall sensitivity of the NSECT system for detection of iron overload in adults may be between 0.5-2 mg/g, which represents a clinically significant and relevant degree of overload. Finally the NSECT system has the potential to develop into a low dose, non-invasive, accurate and sensitive system to detect clinically significant concentrations of iron in adult patients (of different sizes) with liver iron overload.

**5. Future work:**
This study determined that the sensitivity of the system lies in the range of concentrations between 0.5 mg/g and 2 mg/g, which represents a coarse range. We are currently working on obtaining a more precise estimation of the sensitivity using finer increments for the concentration values. In addition, we are also investigating the sensitivity of the system in detecting iron deposited in localized concentrations (i.e., 'lesions') in the liver through an imaging study. This data will be useful in developing NSECT as an imaging modality capable of non-invasively detecting, quantifying and localizing iron deposits in the liver.

**6. References:**

Agostinelli, S. and G. Collaboration (2003). "GEANT4: A Simulation Toolkit." Nuclear Instruments and Methods in Physics Research NIM A **506**: 250-303.

Attix, F. H. (1986). Introduction to radiological physics and radiation dosimetry. New York, Wiley.

Bernardino, M. E. (1984). "Percutaneous biopsy." AJR Am J Roentgenol **142**(1): 41-45.

Floyd, C. E., J. E. Bender, et al. (2006 ). "Introduction to neutron stimulated emission computed tomography." Physics in Medicine and Biology **51**: 3375-3390.

Floyd, C. E., A. J. Kapadia, et al. (2008). "Neutron Stimulated Emission Computed Tomography of a Multi-Element Phantom." Phys Med Biol **53**: 2313-2326.

Gandon, Y., D. Guyader, et al. (1994). "Hemochromatosis: diagnosis and quantification of liver iron with gradient-echo MR imaging." Radiology **193**(2): 533-538.

ICRU (1992). Photon, electron, proton and neutron interaction data for body tissues. ICRU Report 46. Bethesda, MD,, International Commission on Radiation Units and Measurements. **46**.

Ivanchenko, V. N. (2003). "Geant4 toolkit for simulation of HEP experiments." Nuclear Instruments and Methods in Physics Research Section A **502**(2-3): 666-668

Jackson, J. D. (1975). Classical electrodynamics. New York, Wiley.

Kapadia, A. J. (2007). Accuracy and Patient Dose in Neutron Stimulated Emission Computed Tomography for Diagnosis of Liver Iron Overload: Simulations in GEANT4. Biomedical Engineering. Durham, NC, Duke University. PhD.

Kapadia, A. J. (2008). Accuracy and Dose in Neutron Stimulated Emission Computed Tomography: Simulations in GEANT4 (Paperback), VDM Verlag.

Kapadia, A. J., G. A. Agasthya, et al. (2009). Detection of iron overload through neutron stimulated emission computed tomography: a sensitivity analysis study. SPIE Symposium on Medical Imaging, Orlando, FL.

Kapadia, A. J., C. E. Floyd, et al. (2005 ). Non-invasive quantification of iron 56-Fe in beef liver using neutron stimulated emission computed tomography. IEEE Nuclear Science Symposium, Medical Imaging Conference, Puerto Rico.

Kapadia, A. J., B. P. Harrawood, et al. (2008). GEANT4 simulation of NSECT for detection of iron overload in the liver. SPIE Symposium on Medical Imaging, San Diego, CA.

Kapadia, A. J., B. P. Harrawood, et al. (2008). Validation of a GEANT4 simulation of neutron stimulated emission computed tomography. SPIE Symposium on Medical Imaging, San Diego, CA.

Kapadia, A. J., A. C. Sharma, et al. (2007). GEANT4 simulation of an NSECT system for iron overload detection. IEEE Nuclear Science Symposium, Medical Imaging Conference, Honolulu, HI.

Kapadia, A. J., A. C. Sharma, et al. (2006). Non-Invasive Estimation of Potassium (39K) in Bovine Liver Using Neutron Stimulated Emission Computed Tomography (NSECT). IEEE Nuclear Science Symposium, Medical Imaging Conference, San Diego, CA.

Kapadia, A. J., G. D. Tourassi, et al. (2008). "Experimental detection of iron overload in liver through neutron stimulated emission spectroscopy." Phys Med Biol **53**: 2633-2649.

Knoll, G. F. (2000). Radiation Detection and Measurement. Hoboken, NJ, Wiley.

National Nuclear Data Center, B. N. L. (2007). National Nuclear Database NuDat 2.3.

National Nuclear Data Center, B. N. L. (2007). NuDat 2.3.

Powell, L. (2005). Hemochromatosis. Harrison's Principles of Internal Medicine. D. Kasper, Fawci, AS, Longo, DL, Braunwald, E, Hauser, SL, Jameson, JL. NY, McGraw Hill. **2:** 2298-2303.

Powell, L. W. (2002). "Diagnosis of hemochromatosis." Semin Gastrointest Dis **13**(2): 80-88.

Powell, L. W., D. K. George, et al. (1998). "Diagnosis of hemochromatosis." Ann Intern Med **129**(11): 925-931.

RSNA. (2007). "Radiation Exposure in X-ray Examinations." American College of Radiology (ACR) and the Radiological Society of North America (RSNA), from http://www.radiologyinfo.org.

Sharma, A. C., B. P. Harrawood, et al. (2007). "Neutron stimulated emission computed tomography: a Monte Carlo simulation approach." Phys Med Biol **52**(20): 6117-6131.

Taouli, B., R. L. Ehman, et al. (2009). "Advanced MRI Methods for Assessment of Chronic Liver Disease." Am. J. Roentgenol. **193**(1): 14-27.

Tsirigotis P, S. T., Shapira MY, Bitan M, Bloom A, Kiselgoff D, et al. "Peliosis Hepatis following treatment with androgen-steroids in patients with bone marrow failure syndromes." Haematologica **Vol 92**(Issue 11): e106-e110.

Widmaier, E. P., H. Raff, et al. (2008). Vander's human physiology : the mechanisms of body function. Boston, McGraw-Hill Higher Education.

Wood, J. C. (2007). "Magnetic resonance imaging measurement of iron overload." Curr Opin Hematol **14**(3): 183-190.